

RECEIVED MAY 27 2004

W.H. finds fr  
Theme NA

| REPORT DOCUMENTATION PAGE  |  |   | AFRL-SR-AR-TR-04-   |   |
|--|--|---|---|---|
| <p>The public reporting burden for this collection of information is estimated to average 1 hour per gathering and maintaining the data needed, and completing and reviewing the collection of information, including suggestions for reducing the burden, to the Department of Defense. Executives should notwithstanding any other provision of law, no person shall be subject to any penalty for failing to control number.</p> <p><b>PLEASE DO NOT RETURN YOUR FORM TO THE ABOVE ORGANIZATION.</b></p>  |  |   |   |   |
| 1. REPORT DATE (DD-MM-YYYY)<br>18-05-2004  |  | 2. REPORT TYPE<br>Final   | 3. DATES COVERED (From - To)<br>June 2001 - December 2003 |   |
| 4. TITLE AND SUBTITLE<br>Micro-Combustion for Nano and Pico Satellite Propulsion Systems<br><br>05-19-04 AR 0552   |  | 5a. CONTRACT NUMBER<br><br>5b. GRANT NUMBER<br>AFOSR F496200110435<br><br>5c. PROGRAM ELEMENT NUMBER<br><br>5d. PROJECT NUMBER<br><br>5e. TASK NUMBER<br><br>5f. WORK UNIT NUMBER |   |   |
| 6. AUTHOR(S)<br>Cadou, Christopher P.<br>Leach, Timothy T.   |  |   |   |   |
| 7. PERFORMING ORGANIZATION NAME(S) AND ADDRESS(ES)<br>University of Maryland, Department of Aerospace Engineering<br>3181 Glenn L. Martin Hall,<br>College Park, MD 20742  |  | 8. PERFORMING ORGANIZATION REPORT NUMBER  |   |   |
| 9. SPONSORING/MONITORING AGENCY NAME(S) AND ADDRESS(ES)<br>Air Force Office of Scientific Research<br><br>AFOSR /PK ( ATTN: Wendy Veon)<br>4015 Wilson Blvd, Room 173 <i>WA</i><br>Arlington, VA 22203-1954.   |  | 10. SPONSOR/MONITOR'S ACRONYM(S)<br>AFOSR<br><br>11. SPONSOR/MONITOR'S REPORT NUMBER(S)   |   |   |
| 12. DISTRIBUTION/AVAILABILITY STATEMENT<br><br><i>Approved for public release.<br/>distribution unlimited</i>  |  | BEST AVAILABLE COPY   |   |   |
| 13. SUPPLEMENTARY NOTES  |  | 20040617 055  |   |   |
| 14. ABSTRACT<br>The performance of millimeter-scale combustors intended for micro, nano, and pico-satellite propulsion is strongly influenced by heat exchange to and within the combustor structure. The purpose of this work is to develop models for the effects of fluid-structure coupling on combustion in micro-combustors and to develop non-intrusive methods for making measurements of species concentration and temperature that can be used to validate these models. A simple one-dimensional model based on the thermal theory for flame propagation was extended to include the effects of heat exchange with a conductive structure. The important findings were that heat exchange between the gas and structure in micro-combustors can increase the burning rate and the reaction zone thickness. Micro-combustor geometries that maximize power density were identified. The experimental component of the work developed a non-intrusive technique based on infrared absorption spectroscopy that made measurements of temperature and species concentration in a flame stabilized between two silicon plates spaced less than 1 mm apart. |  |   |   |   |
| 15. SUBJECT TERMS<br>Combustion, micro-combustion, propulsion  |  |   |   |   |
| 16. SECURITY CLASSIFICATION OF:<br>a. REPORT U   |  | 17. LIMITATION OF ABSTRACT<br>UU  | 18. NUMBER OF PAGES<br>94                                 | 19a. NAME OF RESPONSIBLE PERSON<br>Christopher Cadou<br><br>19b. TELEPHONE NUMBER (Include area code)<br>301-405-0829 |

**Final Performance Report:  
Micro-Combustion for Nano and Pico Satellite Propulsion Systems**

AFOSR F496200110435

Dr. Mitat Birkan – Program Manager

May 20, 2003

PI: Christopher P. Cadou  
University of Maryland  
Department of Aerospace Engineering  
3179D Glenn L. Martin Hall  
College Park, MD 20742

## Abstract

The performance of millimeter-scale combustors intended for micro, nano, and pico-satellite propulsion is strongly influenced by heat exchange to and within the combustor structure. The purpose of this work is to develop models for the effects of fluid-structure coupling on combustion in micro-combustors and to develop non-intrusive methods for making measurements of species concentration and temperature that can be used to validate these models. A simple one-dimensional model based on the thermal theory for flame propagation was extended to include the effects of heat exchange with a conductive structure. The predictions of the model are in qualitative agreement with the results of one-dimensional numerical simulations with full chemistry that include distributed heat transfer between the reacting gas and the combustor structure as well as heat transfer within the combustor itself. The important findings are that heat exchange between the gas and structure in micro-combustors can increase the burning rate and the reaction zone thickness. Micro-combustor geometries that maximize power density were identified. The experimental work developed two prototype silicon-walled micro-burners for investigating fluid-structure coupling in micro-combustors without having to incur the large costs of microfabrication. A non-intrusive technique based on infrared absorption spectroscopy was used to make measurements of temperature and species concentration in a flame stabilized between two silicon plates spaced less than 1 mm apart. The spatial resolution of the measurements in the streamwise direction was better than 1 mm indicating that it should be possible to observe the reaction zone broadening phenomena and other changes in the structure of the reaction zone associated with micro-scale combustion. This work has generated 1.5 Masters' theses, 4 conference papers, and 3 articles submitted to peer-reviewed journals.

## 1. Introduction

This research investigates the physics of micro-scale fluid-structure coupling in reacting flow systems for the purpose of developing efficient micro-rocket motors. It is motivated by the US Air Force's need in the coming decade for compact propulsion devices suitable for positioning and attitude control of micro-satellites and other micro-scale space vehicles. While there is a range of technologies that are available for this purpose, chemical rockets remain extremely attractive because of the high energy density of their fuels. However, constructing efficient chemical rocket engine combustors becomes difficult as the size of the motor is reduced. The problems stem from the strong coupling between fluid and structure that exists at small scales: Heat loss and radical quenching at the walls makes it difficult to stabilize and sustain efficient combustion. This research program developed appropriate models and acquired preliminary experimental data that will be used to identify the physical parameters and processes that distinguish micro-combustion from combustion at conventional scales. A two-pronged approach was pursued. The modeling and simulation component was used to gain fundamental insight into the physical processes responsible for stabilization of flames in micro-channels. The modeling and simulation was also important for guiding the design of the micro-burner that will be used to evaluate the models' predictions. The experimental component focused on developing the non-intrusive diagnostic tools necessary to make measurements in micro-reacting systems and to validate the predictions of the models and simulations. The modeling and experimental components of the program will be discussed in separate sections.

## 2. Modeling and Simulation

### 2.1 Previous Work

The idea that fluid-structure interaction is important is not new as there is an old and rather extensive literature documenting the importance of heat loss and chemical quenching on flame propagation and extinction [1-4]. While heat exchange with a cold structure can lead to flame quenching, it has been shown experimentally that combustion

in passages smaller than the ‘quenching diameter’ is possible if the wall temperature is high enough [5]. The interest in micro-power/propulsion systems has also motivated theoretical work that focuses on the coupling between the reacting gas and the wall in micro-combustors. Peterson [6] used a basic thermodynamic argument to establish size limits for heat engines in general. In a similar vein, Aichlmayer et al. [7] included thermal coupling between the gas and the structure to identify the minimum practical combustion volume for a miniature HCCI engine. Daou and Matalon [8,9] investigated the effects of velocity, heat loss to the structure, and passage width on premixed flames propagating in channels with constant temperature walls. They showed that burning rate decreased as the heat transfer coefficient between the wall and the environment increased, and that complete extinction or partial extinction at the walls was possible depending on the values of the passage height and the heat loss to the environment. However, heat transfer between the gas and the structure and the structure and the environment were assumed to occur only in a direction perpendicular to the gas flow. Ronney [10] derived a model that used a perfectly stirred reactor to study non-adiabatic combustion in heat-recirculating combustors where heat from the post-flame region is transferred upstream to pre-heat the incoming reactants. This work showed that streamwise heat conduction within the structure of the combustor is a dominating effect at microscale.

Experimental work focused on the development of micro-gas turbine engines has demonstrated stable gas-phase combustion of H<sub>2</sub>-air mixtures [11] and stable catalytic combustion of propane-air mixtures [12] in silicon MEMS combustors with passage heights at or below the gas-phase quenching diameter. Both MEMS combustors,

however, had unacceptably low overall efficiencies. Two main reasons for this were identified: First, and as expected, thermal losses were large because of the large surface to volume ratio of the combustor. Second, and somewhat unexpected, was the observation that the reaction zone in the H<sub>2</sub> combustor appeared to be much thicker than what one would expect for a laminar flame. Often, the flame protruded far outside the combustor suggesting that chemical conversion efficiency was also low in this device.

The theoretical work reported here incorporates the effects of axial heat transfer within the combustor structure in an attempt to explain the apparent broadening of the reaction zone observed in the aforementioned experiments, and to better understand how to determine how long a micro-combustor needs to be. To this end, a simple analytical model is developed to describe how the reaction zone thickness depends on the size of the passage, the thermal properties of the structure and the amount of heat lost to the environment. Heat transfer between the gas and the structure, the structure and the environment, and streamwise heat transfer within the structure itself are all included. The predictions of this model are validated qualitatively via comparison to a more detailed one-dimensional numerical simulation that includes distributed heat transfer between the reacting gas and the structure and thermal exchange within the structure in addition to mass transport and full chemistry.

## 2.2 Simple Analytical Model

Mallard and Le Chatelier's thermal model for flame propagation [13] predicts that the laminar flame speed  $S_L$  is proportional to the square root of the product of the thermal diffusivity ( $k_r/\rho C_p$ ) of the unburned reactants and the chemical reaction rate  $RR$ :

$$S_L = \sqrt{\frac{k_r}{\rho C_p} \frac{T_f - T_i}{T_i - T_0} RR} \quad (1)$$

$T_o$ ,  $T_i$  and  $T_f$  are respectively the temperatures of the unburned mixture, the temperature at ignition, and the temperature of the post-flame gases. The theory applies to free-burning (i.e. unconfined) laminar flames and is predicated on the notion that the flame speed is set by the rate at which heat can diffuse upstream into the unburned mixture.

A more complex picture emerges, however, when the theory is extended to include an additional heat exchange path through the structure from the post-flame region upstream to the pre-flame region (figures 1 and 2). The thermal resistor network of figure 3 can be used to visualize the heat exchange between the reaction zone and the preheat area as well as the heat loss to the environment. In the figure,  $\dot{q}_{gen}$  is the rate of heat generation by the reaction,  $\dot{q}_{loss}$  is the rate at which heat is lost to the environment by convective heat transfer from the plates,  $T_e$  is the environment temperature,  $T_s$  is the structure temperature and  $T_f$  is the flame temperature.  $R_r$  and  $R_s$  are the resistances to conductive heat transfer in the gas and the structure respectively and  $R_{bl}$  is the resistance to convective heat transfer from the gas to the structure through the boundary layer. These thermal resistances can be expressed as follows:

$$R_r = \frac{\delta_r}{k_r A_r}, \quad R_s = \frac{\delta_r}{k_s A_s}, \quad R_{bl} = \frac{2H}{k_r Nu A_r} \quad (2)$$

where  $k_r$  and  $k_s$  are the thermal conductivity of the gas and of the structure respectively,  $\delta_r$  is the reaction zone thickness,  $H$  is the passage height,  $Nu$  is the Nusselt number and  $A_r$  and  $A_s$  are the cross-sectional surface areas for conduction in the gas and the structure respectively. Note that the definition of  $R_{bl}$  assumes that the surface area for convective heat transfer is on the order of the surface area for conduction in the gas.

In the adiabatic case,  $\dot{q}_{loss}$  is set to 0 and since the flame temperature is a constant equal to the adiabatic flame temperature, the rate at which heat is generated by the flame ( $\dot{q}_{gen}$ ) does not need to be defined. Further assuming that  $\delta_r = S_L/RR$  leads to the following expression for the reaction zone thickness:

$$\delta_r = \sqrt{\beta \frac{k_r}{\rho C_p} \frac{T_f - T_i}{T_i - T_0} \frac{I}{RR}} \quad (3)$$

Beta ( $\beta$ ) is a parameter that accounts for the variation of the overall thermal resistance of the gas-structure combination as a function of the passage height  $H$ , the ratio  $\zeta$  of the cross sectional areas for axial conduction in the structure and the reactant stream-tube ( $\zeta = A_s/A_r$ ) and the ratio  $\lambda$  of the thermal conductivity of the structure and that of the reactive mixture ( $\lambda = k_s/k_r$ ).

$$\beta = \frac{1 + \zeta \lambda \left( 1 + \frac{2H}{\delta_r} \frac{I}{Nu} \right)}{1 + 2\zeta \lambda \frac{H}{\delta_r} \frac{I}{Nu}} \quad (4)$$

For a rectangular channel,  $\zeta = 2t/H$  where  $t$  is the thickness of the combustor wall. Combining equations 3 and 4 to solve for  $\delta_r$  results in a third order algebraic equation with three possible solutions. Of these, only one value of  $\delta_r$  is positive and hence physically realistic.

Equations 3 and 4 indicate that the reaction zone thickness depends on the normalized thermal conductivity of the structure, the area ratio for axial conduction  $\zeta$ , the passage height  $H$ , and the Nusselt number in addition to the usual parameters associated with the Mallard-Le Chatelier theory. While equation 3 is an implicit expression for  $\delta_r$  because  $\beta$

is a function of  $\delta_r$ , we can check that it has the proper asymptotic behavior using equations 3 and 4. At zero Nusselt number or infinite passage height, equation 3 indicates that  $\beta \rightarrow 1$ . Inserting this result into equation 4 recovers the traditional formulation in which the reaction zone thickness only depends on the thermal diffusivity of the gas. Conversely, at large Nusselt numbers or small passage heights, equation 3 indicates that  $\beta \rightarrow 1 + \zeta \lambda$ , which is always greater than one. This indicates that the reaction zone thickness increases, leading to a flame broadening. At large Nusselt numbers, the thermal resistance between the gas and the structure is small and the transport of heat (and hence the reaction zone length) is determined by the thermal resistance of the structure acting in parallel with the thermal resistance of the gas. As a result, in either the large Nusselt number or the small passage height limits, the reaction zone thickness is determined by the thermal conductivity of the structure and the gas, and the relative areas for axial heat conduction.

Note also that since the laminar flame speed is directly proportional to the flame thickness, the simple model predicts that the evolution of  $S_L$  with passage height follows the same trend as  $\delta_r$ , with the burning rate increasing as the passage height is reduced. This occurs because the conductive structure allows heat from the post-flame to be transferred upstream to the reactants. This increase in burning rate is also consistent with well known work on the effects of pre-heating reactants in laminar flames [14], and the pre-heating mechanism is very similar to that occurring in ‘excess enthalpy’ burners [15,16] where increases in burning rate are also observed.

The effect of heat loss to the environment, an important consideration in ‘micro-combustors because of their large surface/volume ratios, can be incorporated by adding a

heat sink to the thermal network and by recognizing that the chemical reaction acts like a heat (or analogous current) source. In this case,  $\dot{q}_{gen}$  is computed by adjusting the rate of heat generation in the adiabatic case  $\dot{q}_{ad}$  by a factor that accounts for the effect of an arbitrary flame temperature  $T_f$

$$\dot{q}_{gen} = \dot{q}_{ad} \exp\left(-\frac{E_a}{RT_f} + \frac{E_a}{RT_{f,ad}}\right) \quad (5)$$

where  $E_a$  is the activation energy,  $R$  is the gas constant and  $T_{f,ad}$  is the adiabatic flame temperature. The value for  $E_a$  corresponds to a one-step overall reaction mechanism for stoichiometric H<sub>2</sub>-air combustion and was taken from [17].  $\dot{q}_{loss}$  is expressed as a convective heat loss:

$$\dot{q}_{loss} = h_{Te} A_{loss} (T_s - T_e) \quad (6)$$

where  $h_{Te}$  is the coefficient for heat transfer from the plates to the environment and  $A_{loss}$  is the surface area for convective heat loss. Since heat loss occurs mainly in the region where the gas temperature is high, the area for heat loss is assumed to correspond to a length equal to the flame thickness. The heat transferred from the reaction zone to the preheat zone is written as the difference between the heat generated by the reaction and the heat lost to the environment:

$$\dot{q} = \dot{q}_{gen} - \dot{q}_{loss} \quad (7)$$

Equation 7 is used to compute an ‘effective’ flame temperature which includes the effect of heat loss.

$$T_f = T_i + \dot{q} R_{eff} \quad (8)$$

In this expression,  $T_i$  is the ignition temperature and  $R_{eff}$  is the effective thermal resistance of the thermal network defined as:

$$R_{eff}^{-1} = R_r^{-1} + (R_s + 2R_{bl})^{-1} \quad (9)$$

Balancing the heat fluxes through the boundary layer, structure, and to the environment leads to the following expression for the peak temperature of the structure  $T_s$ :

$$T_s = T_i + (T_f - T_i) \frac{R_s + R_{bl}}{R_s + 2R_{bl}} - \dot{q}_{loss} \frac{R_r(R_s + R_{bl})}{R_r + R_s + R_{bl}} \quad (10)$$

As before, performing a thermal balance on the entire network gives an expression for the flame thickness:

$$\delta_r = \frac{\dot{q}}{\rho C_p (T_i - T_0) RR} \quad (11)$$

The reaction rate in equation 11 is the adiabatic reaction rate adjusted by a factor accounting for the flame temperature  $T_f$

$$RR = RR_{ad} \exp\left(-\frac{E_a}{RT_f} + \frac{E_a}{RT_{f,ad}}\right) \quad (12)$$

The system of equations {5-12} can be solved using an iterative procedure and an initial guess that corresponds to the adiabatic case:

$$\begin{cases} T_f = T_{f,ad} \\ \dot{q} = \dot{q}_{ad} \end{cases} \quad (13)$$

### 2.3 Numerical Model

A transient 1-D model developed by Zhu and Jackson for studying the performance of catalytic reactors is adapted to study the behavior of a flame stabilized in a channel. A complete description of the code may be found in [18] and only an abbreviated description is presented here.

For the numerical model in this study, all surface chemistry is removed from the calculations and as such there is no mass exchange between the surface and the gas

phase. Further, the pressure in the channel flow is assumed constant, which implies that the momentum equation is neglected entirely and velocity is calculated from mass conservation. While this is appropriate for the purposes of comparison with the analytical model, the pressure drop in micro-channels can be a significant performance parameter because of its impact on the efficiency of thermodynamic cycles. However, since pressure losses relative to total pressure are relatively small for any practical implementation of a thermodynamic cycle, pressure losses are assumed to be small and are neglected.

The numerical model divides the channel into axial cells and solves for the following variables in each cell:  $\rho$ ,  $u$ ,  $T$ ,  $T_s$ , and  $Y_k$  where  $Y_k$  is the vector of mass fractions for the species in the gas phase. The governing equations in each cell for these variables include the following:

- ideal gas law,

$$\rho = \frac{PW_m}{RT} \quad (14)$$

- conservation of mass,

$$\frac{d(\rho u)}{dx} = \rho \sum_k \left( \frac{W_m}{W_k} \frac{dY_k}{dt} \right) + \frac{\rho}{T} \frac{dT}{dt} \quad (15)$$

- conservation of energy in the gas-phase

$$\rho C_P \frac{dT}{dt} = -\rho u \frac{d}{dx} \left( \sum_k (h_k Y_k) \right) + \frac{d}{dx} \left( k_r \left( \frac{dT}{dx} \right) \right) - a_{ch} h_T (T - T_s) - \sum_k (W_k h_k \dot{\omega}_k) \quad (16)$$

- conservation of species in the gas-phase,

$$\rho \frac{dY_k}{dt} = \frac{d}{dx} \left( \rho D_k \frac{dY_k}{dx} \right) - \rho u \frac{dY_k}{dx} + W_k \dot{\omega}_k \quad (17)$$

- and conservation of energy in the solid structure,

$$\rho_s C_{P,s} \frac{dT_s}{dt} = \frac{d}{dx} \left( k_s \left( \frac{dT_s}{dx} \right) \right) + a_s h_T (T - T_s) - a_s h_{T,e} (T_s - T_e) \quad (18)$$

In the above equations,  $W_m$  is the mean molecular weight of the gas flow,  $\omega_k$  is the production rate of the  $k^{\text{th}}$  species in the gas phase and  $a_{ch}$  is the surface area of the channel per unit channel volume.

For the numerical model, a 9-species, 19-reaction mechanism [19] for H<sub>2</sub>-air combustion is employed. Properties for the gas-phase varied with temperature were based on fitted polynomials ( $h_k$  and  $C_P$ ) and on kinetic theory approximations ( $k_r$  and  $D_k$ ). The properties for the solid structure ( $\rho_s$ ,  $C_{P,s}$  and  $k_s$ ) did not vary with temperature in the numerical model.

The boundary conditions for equations 15-18 in the numerical model are as follows:

- at  $x = x_{\text{in}}$ ,

$$\begin{cases} u = u_{in} \\ Y_k = Y_{k,in} \\ \rho u \bar{C}_P (T - T_{in}) = \zeta h_{T,in} (T_s - T) \\ h_{T,in} (T_s - T) = k_s \left( \frac{dT_s}{dx} \right) \end{cases} \quad (19)$$

- and at  $x = x_{\text{out}}$ ,

$$\begin{cases} \frac{dY_k}{dx} = 0 \\ k_r \left( \frac{dT}{dx} \right) = 0 \\ k_s \left( \frac{dT_s}{dx} \right) = 0 \end{cases} \quad (20)$$

For the inlet boundary at  $x = x_{\text{in}}$ ,  $h_{T,in}$  represents the effective heat transfer coefficient to the upstream portion of the gas flow, and for the current study  $h_{T,in} = 0$  such that  $T = T_s =$

$T_{in}$  for the first cell boundary. For all runs in the current study,  $T_{in} = 300$  K, and  $Y_{k,in}$  are set for a H<sub>2</sub>-air mixture with a  $\Phi = 1.0$ .  $P = 1.0$  atm. for all simulations. The value for  $u_{in}$  is determined during a model run as discussed below to ensure that the flame stabilization occurred away from the reactor inlet and thereby flame thicknesses were found independent of the inlet boundary conditions.

A discretized version of equations {14-18} is solved simultaneously on an evenly spaced grid consisting of 201 elements with a domain length of 1.0 cm and the boundary conditions shown in equations 19-20. Adequate grid resolution has been verified by doubling the number of grid points and finding that flame thicknesses did not change from the 201-cell simulation. The 1.0 cm computational domain was sufficient to contain the reaction zone for all runs presented here. The code uses the method of lines to implement an adaptive time step. The convective terms are discretized using a Godunov-type upwind finite volume method while a central difference method was used to discretize the diffusive terms. The resulting set of discrete equations was integrated using the stiff PDE solver LIMEX [20].

The numerical solution depends strongly on user-specified parameters including  $H$ ,  $Nu$ ,  $k_s$  and  $h_{T,e}$ , and for a given combination of user-defined parameters, the necessary  $u_{in}$  ( $\approx S_L$ ) to stabilize the flame in the domain away from the inlet boundary is unknown. Conventional flame models have used the approach of solving the steady-state version of equations {14-18}, fixing a temperature within the computational domain, and solving for  $\rho u$  as an eigenvalue for the system [21]. However, in the current study, it is desired to model conditions when the flame undergoes extinction, and thus rather than anchoring the flame with a fixed temperature in the mesh, an alternative approach based on the

transient integration of equations {14-18} is implemented. An initial condition is set with a  $T$  and  $T_s = 1000$  K throughout the domain and  $u_{in}$  to a value below the expected  $S_L$ . A steady solution is found typically after 10 s of transient integration and the flame is anchored at the inlet of the reactor.  $u_{in}$  is then increased by 0.1% and the solution is recalculated. This process is repeated until the induction zone length (based on the decay of the O<sub>2</sub> mass fraction in the flame zone) equals that calculated for the freely propagating flame. The value for the laminar flame speed associated with a freely propagating flame was found in [22] and equaled 2.1 m/s at the equivalence ratio considered here. At the final  $u_{in}$ , the integration continues for 100 s to ensure that the final solution is at a steady-state condition.

Upon determining the final solution at a value of  $u_{in}$  that provides a reaction zone away from the inlet, the flame thickness can be determined. The definition of flame thickness proposed by Sung and Law [23] is used where the flame thickness is the ratio of the total temperature difference to the maximum value of the temperature derivative:

$$\delta_r = \frac{T_f - T_0}{\left(\frac{dT}{dx}\right)_{\max}} \quad (21)$$

For H<sub>2</sub>-air mixtures with  $\Phi = 1.0$  and  $T_0 = 300$  K, the flame thickness for a freely propagating flame computed using equation 19 is 0.42 mm and is consistent with values reported elsewhere [24]. For the same flame, the total temperature change across the flame is  $T_f - T_0 = 2036$  K. This is 61 K lower than the difference associated with complete combustion by an adiabatic flame. This reduced temperature difference is the result of dissociation.

## 2.4 Results and Discussion

### 2.4.1 Comparison of Analytical Model and Numerical Simulations

Figure 4 is a plot of the non-dimensional flame broadening (i.e. the ratio of the reaction zone of thickness  $\delta_r$  to the reaction zone thickness associated with a freely propagating flame in the absence of the structure  $\delta_{r,fr}$ ) as a function of the normalized passage height  $H/\delta_{r,fr}$  for four values of  $Nu$  under adiabatic structure conditions (i.e.,  $h_{T,e} = 0$ ). Note that the value of  $\delta_{r,fr}$  found using the numerical simulation is 0.42 mm. The solid lines without symbols correspond to the simple analytical model while the dotted lines with symbols correspond to the numerical simulations. The analytical and numerical models have good *qualitative* agreement as both indicate that  $\delta_r$  undergoes a limit cycle behavior with variations in  $H$ . At large  $H$ ,  $\delta_r/\delta_{r,fr} = 1$  and  $\delta_r$  is determined by  $k_r$  (~0.2 W/mK). As  $H$  decreases,  $\delta_r$  becomes more strongly influenced by the structure thermal conductivity  $k_s$  (10 W/mK). In both models, the strength of the thermal coupling between the fluid and the structure (determined in part by  $Nu$ ) determines at what  $H$  the transition from gas to structure-dominated heat transfer occurs. The transition begins to occur as  $H$  decreases below  $10\delta_{r,fr}$  (~5 mm) and the broadening has reached its maximum limit when  $H < 0.01\delta_{r,fr}$  the unconfined flame thickness. Many factors contribute to the discrepancy in the amplitude of the broadening predicted by the numerical and analytical models. Some important differences include the use of multi-step versus single step chemistry, variable versus fixed gas-phase properties, and the use of discrete versus distributed heat transfer between the gas and the structure.

Figure 5 compares analytical and numerical predictions of the ratio of the flame broadening  $\delta_r/\delta_{r,fr}$  as a function of the normalized passage height  $H/\delta_{r,fr}$  for three values of  $k_s$ . Both the model and the simulation show that the broadening depends on  $k_s$ . Increasing  $k_s$  increases the heat transfer rate through the structure, which thereby reduces the necessary heat transfer rate through the gas phase. This enables the temperature gradient through the gas to be shallower and allows the reaction zone thickness to be longer than that required for a freely propagating flame. While both models show that the passage height corresponding to the transition from gas to structure-dominated thermal exchange does not depend strongly on  $k_s$ , the amplitude of the broadening phenomenon appears to be a stronger function of the thermal conductivity of the structure in the analytical model than in the numerical model.

The general effect of axial conduction is illustrated further in figure 6, which shows the non-dimensional flame broadening as a function of the non-dimensional thermal conductance ( $\lambda\zeta$ ) of the structure for three values of  $H/\delta_{r,fr}$ . Both the analytical model and numerical simulation indicate that the increase in the reaction zone thickness approaches a limit with increasing conductance of the structure. This limit depends on  $Nu$  as well as  $H$ . For a highly conductive structure, the resistance to heat transfer at the gas/structure interface limits flame broadening. The magnitude of broadening predicted at the high structure conductance limit by the analytical model is approximately 30% less than that predicted by the numerical simulation, but both show similar limit cycles.

The results for the adiabatic structure cases in figures 4-6 indicate that conduction of heat from the post-flame through the structure to the upstream preheat zone can broaden the reaction zone by a factor of 4 or more. Limits associated with the thermal resistance

between the gas flow and the structure limit heat transfer upstream and in turn limit the magnitude of the broadening phenomenon.

Besides increased heat transfer into the structure from the flame, heat loss from the structure to the environment is also important in micro-scale combustors and can lead to flame quenching. Figure 7 shows the non-dimensional flame broadening as a function of the normalized passage height for three values of  $h_{T,e}$  for both the analytical model and the numerical simulation. For  $h_{T,e}$  of  $O(1)$  or less, reaction zone broadening arises as before, but as  $H$  decreases the heat loss to the environment eventually leads to a reduction in the flame zone thickness followed by extinction. Extinction occurs when heat loss to the environment prevents sufficient thermal feedback to the preheat zone to sustain continuous ignition of the flame. As  $h_{T,e}$  increases to large values  $\sim 1.0$ , the broadening phenomenon is replaced by a rapid reduction of the flame thickness with decreasing  $H$  and flame extinction occurs at relatively large  $H$ . The reduction in reaction zone thickness with decreasing  $H$  for structures with large thermal losses arises because steeper temperature gradients in the gas and structure must be sustained in order to transfer an adequate fraction of the reaction heat release back to the preheat zone.

While the qualitative agreement between the analytical and numerical models lends credence to the principles underlying the modified Mallard-Le Chatelier theory, the quantitative discrepancy between the analytical model and numerical simulation is hardly surprising. As indicated earlier, the discrepancy can arise from numerous factors including the implementation of variable properties and multi-step chemistry in the numerical model. In addition, the single-step chemistry of the analytical model assumes that the reaction goes to completion while the multi-step chemistry of the analytical

model accounts for dissociation and the accompanying reduction in flame temperature. Finally, the numerical model distributes the heat feedback from the structure throughout the reaction and preheat regions. This reduces to some extent the impact of the structural heat feedback in comparison to the analytical model which sends the structural heat transfer entirely back to the preheat zone.

#### 2.4.2 Implications for Power Density

While the broadening phenomenon is of interest theoretically, it also has very practical implications on the development of high power density combustors. For the purpose of this work, the power density is defined as follows:

$$\dot{w}_D = \frac{\dot{W}}{V} \quad (22)$$

where  $\dot{W}$  is the power generated by the combustion process and  $V$  is the volume of the combustor in which the chemical energy is released. We have already shown that thermal exchange with the structure increases the reaction zone thickness and this observation along with equation 22 indicates that the overall power density of the combustor might decrease as the size of the combustor is reduced. This, of course, would run counter to the objective of miniaturizing combustors in the first place, which is to increase power density. However, as will be noted below, the increased heat feedback from the structure to the preheat zone results in a substantial increase in the allowable burning velocity. This tends to offset the increase in the necessary volume, and results in a maximum in  $\dot{w}_D$  at intermediate combustor channel heights.

Due to the complex coupling of the structure with the heat transfer to the upstream zone of the flame, maximizing power density,  $\dot{w}_D$ , requires a careful optimization over the structure properties (geometric as well as thermophysical). Results of a general

optimization will be presented later, but to provide some insight into the effects of channel height on  $\dot{w}_D$ , it has been calculated for the 1 cm passage lengths presented so far by using the following equation:

$$\dot{w}_D = \frac{\rho S_L \int_{T_0}^{T_f} C_p(T) dT}{2\delta_r + l_{ind}} \quad (23)$$

Equation 23 relies on the approximation that the total length required to complete combustion is two times the reaction zone thickness ( $\delta_r$ ) plus the induction length ( $l_{ind}$ ).

Figure 8 is a sample calculation showing the evolution of the ratio of  $\dot{w}_D$  for a range of  $H$  to the  $\dot{w}_D$  for the unconfined flame. The cases presented in figure 8 are for an adiabatic structure and fixed values of  $Nu$ ,  $\zeta$ , and  $\lambda$ . The plot suggests that as  $H$  decreases and approaches the order of the flame thickness,  $\dot{w}_D$  increases toward a maximum. As  $H$  decreases further then,  $\dot{w}_D$  begins to decrease toward a limit that is greater than in the unconfined case as the passage height is reduced further. Note that in the analytical model,  $S_L$  is proportional to  $\delta_r$ , and thus, there is no change in power density as passage height is reduced.

Figure 9 shows that the interesting behavior of  $\dot{w}_D$  vs.  $H$  results from the fact that as  $H$  decreases,  $S_L$  begins to increase before  $\delta_r$ . This causes the power density to increase over the value associated with the freely propagating flame. As  $H$  is decreased further, the flame does begin to broaden, and the power density drops off but it still remains above the power density associated with the freely propagating flame. This result shows the potential benefits of micro-scale combustors and illustrates the possibility of optimizing combustor geometries for a specific design application.

#### 2.4.3 Additional Silicon Constraints

The use of silicon as a combustor material imposes two additional constraints on the simulation that should be included before a complete optimization is performed. The first is that the equivalence ratio be less than or equal to 0.5 so that the adiabatic flame temperature remains below the melting point of silicon (1680K). The second is that the temperature dependence of silicon's thermal conductivity be included. Figure 10 shows that silicon's thermal conductivity changes by more than a factor of five over the expected range of temperatures. As a result, we use a power law fit to tabulated data [25] to represent Silicon's thermal conductivity in the simulations.

#### 2.4.4 Flame Stabilization in Micro-Channels

Figure 11 is a plot of non-dimensional inlet velocity versus non-dimensional passage height for two non-dimensional channel lengths. First, note the increase in flame speed (burning rate) as the channel height is reduced. Second, note that at large passage heights where thermal coupling with the structure is weak, the blow-off and flashback velocities converge to the flame speed associated with a freely propagating flame. As the passage height is reduced and the strength of the coupling between the reacting fluid and the micro-channel structure increases, the blow-off and flashback limits diverge and it becomes possible to stabilize a combustion wave over a range of inlet velocities. Third, note that decreasing the passage length tends to decrease the magnitude of the flame speed increase associated with decreasing passage height, and reduces the difference between the blow-off and flashback limits.

The reasons for these observations can be inferred from figure 12 which shows axial profiles of non-dimensional temperature and major species mass fractions at inlet velocities corresponding to blow-off and flashback. The profiles indicate that the flame is stabilized near the channel exit at the blow-off limit while it is stabilized near the channel entrance at the flashback limit. The flame speed is higher when the flame is stabilized at the channel exit because there is more surface area for heat exchange between the structure and the reactants, and hence more pre-heating of the mixture before reaction occurs. Decreasing the overall length of the combustor reduces the surface area for heat exchange between the structure and the reactants, reduces the pre-heating of the mixture, and thus reduces the flame speed. The blow-off and flashback limits come together as the channel length is reduced because decreasing the length of the micro-channel decreases the range of possible stable flame locations within the channel. This, in turn, decreases the range of stable inlet velocities.

It is interesting to note that the temperature profiles presented in figure 12 do not show the temperature overshoot characteristic of excess enthalpy burners. This is because the profiles in figure 12 correspond to relatively small passage heights where the heat transfer coefficient is large and thermal equilibrium between the gas and the structure is established very quickly. This is consistent with the results of Takeno [16] which show a reduction in the thermal overshoot when the thermal coupling between the gas and the structure is strong. Thermal overshoot *is* observed at larger passage heights where the thermal coupling is weaker and thermal equilibrium takes longer to establish. The physical bases for the ‘smoothing out’ of temperature and species gradients in micro-scale systems have been discussed by Pello [26].

#### 2.4.5 Micro-Combustor Efficiency

Thermal coupling between the reacting gas and the structure has important implications for the design of efficient, high power density combustors. The overall efficiency of a micro-channel combustor can be written as the product of a chemical efficiency and a thermal efficiency:

$$\eta_o = \eta_{ch}\eta_{th} \quad (24)$$

The chemical efficiency is defined as the ratio of the total heat evolved in the reaction to the total heat available if the reaction were to go to completion. In this work, we assume that this is equivalent to the fraction of H<sub>2</sub> that gets consumed before the mixture exits the micro-channel:

$$\eta_{ch} = \frac{\text{Total heat evolved by rxn.}}{\text{Maximum heat available}} = 1 - \frac{Y_{H_2,out}}{Y_{H_2,i}} \quad (25)$$

The thermal efficiency is defined as the ratio of the total heat actually delivered to the flow exiting the channel divided by the total heat evolved by the reaction. This is computed from the axial temperature profile through the micro-channel, the heat loss to the environment, and the mass flow rate:

$$\begin{aligned} \eta_{th} &= \frac{\text{Total heat delivered to flow}}{\text{Total heat evolved by rxn}} \\ &= \frac{\int_{T_i}^{T_{out}} C_p(T) dT}{\int_{T_i}^{T_{out}} C_p(T) dT + \dot{q}_{loss}/\dot{m}} \end{aligned} \quad (26)$$

#### 2.4.6 Optimum Micro-Combustor Geometries

The solid contours in figure 13 show maximum non-dimensional power density as a function of micro-channel length and height for H<sub>2</sub>-air combustion at an equivalence ratio of 0.5, atmospheric pressure, and no heat loss to the environment. Channel height and

length are non-dimensionalized by the reaction zone thickness of a freely propagating H<sub>2</sub>-air flame. Power density is non-dimensionalized with respect to a reference value associated with combustion in a channel where  $L$  and  $H$  equal 1 cm. This reference channel is sufficiently large that there is essentially no influence of the structure on the combustion process. Note that the maximum power density associated with a particular combustor design (i.e.  $L$  and  $H$ ) occurs when the inlet velocity is at the blow-off limit.

Figure 13 shows that there is an optimum micro-channel length where power density is maximized. The maximum is a direct consequence of thermal exchange within the structure. It arises from a competition between the decrease in channel volume and the decrease in flame speed (and hence energy release rate) as the length of the combustor is reduced. The figure shows that thermal exchange within the channel wall makes it possible to achieve power densities in excess of 60 times the maximum associated with the reference channel ( $H=1\text{cm}$ ,  $L=1\text{cm}$ ). Note that the power density also decreases as the channel height is increased. This is because increasing the channel height reduces the thermal coupling between the fluid and the micro-channel wall.

The dashed contours in figure 13 show the overall efficiency of the micro-channel combustor as a function of channel height and length. Since the combustor is adiabatic, the thermal efficiency is 100% and changes in overall efficiency are entirely the result of changes in chemical efficiency. The figure shows that power density and chemical efficiency trade against each other: Attempts to increase power density by decreasing the length of the channel reduce the degree of chemical conversion by decreasing the time available to complete chemical reaction. The figure also shows that heat exchange with

the structure drives the configurations associated with maximum efficiency versus maximum power density farther apart.

Thermal efficiency also changes with combustor configuration when heat loss to the environment is included. Figure 14 shows that heat loss, simulated by introducing a heat transfer coefficient of  $1 \text{ W/m}^2\text{K}$  between the micro-channel and the environment, eventually quenches reaction as channel height is reduced. One would expect similar behavior as channel length is reduced because of reduced chemical efficiency. These effects are observed in figure 15 as the contours of overall efficiency (dashed lines) shift upward and to the right. The subsequent reduction in overall efficiency that arises from heat loss at small passage heights reduces the power density and creates the global maximum in power density shown in the solid contours. There is now a single, optimum, combination of  $L$  and  $H$  that maximizes power density. Not surprisingly, the maximum power density and the efficiency at this point are somewhat lower than those in the adiabatic case. It is important to note that the non-adiabatic power density is only slightly less than the adiabatic value because the heat transfer coefficient, is very small. In practice, one would expect heat losses to be much larger and the maximum realizable power density to be much lower.

Figure 16 is a plot of power density and efficiency at a combustor pressure of 5 atmospheres under non-adiabatic conditions. It shows that increasing the pressure increases the maximum power density and reduces the values of  $L$  and  $H$  associated with the optimum. The reason for this is that the reaction zone thickness decreases with increasing pressure. The power density increases because the flame speed is higher and because an acceptable level of chemical conversion can be achieved in a smaller volume.

Note that an increase in flame speed with pressure is consistent with mixtures having burning velocities greater than 50 cm/s [27]. In these flames, temperatures are high enough that dissociation is important. Increasing the pressure represses dissociation, steepens the temperature profile, and increases the burning velocity [1]. Since thermal feedback to the pre-flame through the micro-channel structure tends to increase the mixture temperature, one would expect flames stabilized in micro-channels to be more sensitive to pressure than freely propagating flames.

Figure 16 also shows that increasing the pressure increases the overall efficiency at the maximum power density point. The reason for this is that the wall temperature, and hence the heat loss from the micro-channel to the environment, remains approximately constant as the pressure is increased. This increases the thermal efficiency by decreasing the ratio of the heat lost to the heat produced.

The results of the power density and efficiency calculations are summarized in Table I and show that the reaction zone thickness doesn't change much as pressure is increased from 5 to 10 atm. As a result, the optimum channel length and height associated with the maximum power density remains approximately constant. It is important to point out that the optimum values of  $L$  and  $H$  listed in table I are estimated using the contour plots and are not the result of an optimization in  $L$  and  $H$ . Since the peaks in power density are relatively flat, the uncertainty in the optimum values of  $L$  and  $H$  is relatively large. As a result, we are unable to make precise estimates of the optimum combustor volume per unit channel depth and the values in the last row of table I are included only as general references.

Finally, it is important to note there are other factors that are important to the design of optimum micro-combustors that have not been discussed here. The first is the conductance (the product of the thermal conductivity and the cross-sectional area) which limits upstream heat conduction through the structure. In this work, the ratio of the wall thickness to the passage height is fixed at  $\frac{1}{2}$ . If this value were made very small, no thermal feedback would occur and hence no optimum power density configuration would be observed. Similarly, making this parameter very large would increase the power density at the optimum until a limit imposed by the heat transfer coefficient between the gas and the structure is reached. The second factor is the pressure drop which is a very important consideration when integrating a combustor into a power cycle. The pressure drop cannot be determined using the present one-dimensional formulation that does not include the momentum equation. However, we have used a simple Poiseuille flow approximation to provide an estimate. Pressure drops near the optimum in figure 15 are about 10% or less. This indicates that combustors designed to be at or near the optimum power density configuration could be integrated into practical power systems.

## 2.5 Conclusions from Modeling and Simulation Efforts

A simple model based on a thermal resistance network has been developed to extend Mallard-Le Chatelier theory to describe a premixed flame propagating in and exchanging heat with a thermally conducting channel. In spite of its simplicity, comparison to the results of a more detailed numerical simulation with axially distributed heat transfer and full chemistry indicate that the simple model captures some of the important aspects of micro-scale combustion as a function of channel height.

Limiting behaviors at small and large channel heights are observed for both the analytical and numerical models. Both models predict the same range of heights for the transition between the two limits. The maximum limit of flame broadening at very small heights is predicted within a factor of two by the analytical model in comparison with the numerical simulation. The length scale associated with quenching due to external heat loss of the structure is not as well predicted, but is still predicted within a factor of 10 of the numerical simulation. Because flame speed and broadening are directly proportional to each other in the analytical model, it cannot be used to predict optimal power densities. However, results from the numerical simulation indicate that fluid-structure coupling can be used to increase a combustor's power density and that there is a passage height where power density is maximized. This occurs because pre-heating the incoming reactants via axial heat transfer increases the reaction rate more than the reaction zone thickness. The net result is an increase in power density.

Axial heat transfer through the structure also provides a mechanism for flame stabilization and the maximum power density for a particular combustor design (values of  $L$  and  $H$ ) occurs at the blow-off limit. Heat transfer from the structure to the environment places a lower limit on the combustor volume that tends to decrease with increasing pressure. The combustor design that maximizes power density generally does not maximize efficiency. However, operation at elevated pressures tends to improve overall efficiency by increasing the burning rate and decreasing the reaction zone thickness.

In summary, axial heat transfer through the structure, in addition to heat loss to the environment, has important effects on the stability and performance of micro-combustors and should be included when estimating micro-combustor performance. The results

presented here demonstrate the utility of the simple analytical model and the importance of fluid-structure coupling in micro-combustion. Acquiring experimental data to validate the predictions of the models will provide valuable information to developers of microscale combustion systems and this endeavor is discussed in the following section.

### 3.0 Micro-Combustion Experiments

#### 3.1 Introduction

The results of the previous section require experimental validation. Unfortunately, however, probing the flow using conventional physical devices like thermocouples and sampling probes is difficult if not impossible in micro-scale combustors. For example, even the bead diameter of the smallest thermocouples can be of the same order of magnitude as the passage height in some of these micro-reacting flows. While it is possible to microfabricate certain sensors like thermocouples in-situ [28], these devices are unable to survive combustion temperatures and require tremendous efforts on the manufacturing side in order to develop and install. Similarly, outfitting a micro-combustor with appropriate optical access is difficult as conventional manufacturing techniques cannot be used to cut holes, install windows, and seal them. Installation of windows and other modifications required to serve the needs of a particular diagnostic technique has the additional disadvantage of significantly changing the thermal properties of the structure. As a result, an instrumented micro-combustor may not perform in very different ways than a non-instrumented one. What would be ideal is a technique that is capable of making non-intrusive measurements of species concentration and temperature without having to modify the micro-device in any way.

The fact that Silicon is transmissive in the mid-infrared wavelengths [29-32] (see figure 17) suggests that it may be possible to use infrared absorption spectroscopy to look through the silicon structure and measure the absorbance of the gas contained in passages within the structure *without modifying it in any way*. The change in absorbance with wavelength can, in turn, be used to infer gas-phase species concentration and temperature. The objective of this component of the research program, therefore, is to demonstrate the viability of this concept and to develop the technique to the point that it may be used to validate the predictions of the modeling and simulation results presented in the previous section. We will focus on making infrared absorption measurements of three species: CO, CO<sub>2</sub>, and C<sub>3</sub>H<sub>8</sub>. The changes in the concentrations of these species with downstream distance will provide a measure of reaction zone thickness, and the rotational structure of CO or CO<sub>2</sub>, will be used to infer temperature. Taken together, the measurements will be used to validate the predictions of the models developed in section 2.

### 3.2 Previous Work (Diagnostics)

While there are relatively many examples of particle image velocimetry (PIV) performed at the micro-scale [33,34], to this researcher's knowledge there are no examples of non-intrusive temperature or concentration measurements made by making measurements through silicon walls. Further, the only attempt to exploit the infrared transparency of silicon involved velocity measurements using PIV [35]. Infrared absorption spectroscopy, on the other hand, is an extremely well developed area and is the subject of many textbooks [36]. Inferring temperature from the rotational spectrum is

also well known but most applications probe only two rotational lines (often using narrow-band IR lasers) and infer temperature from the ratio of the line intensities [37].

### 3.3 Modifications to experiments originally proposed

#### 3.3.1 Diagnostic Technique

In the original proposal, we planned to purchase special-purpose infrared lasers and detectors to measure the infrared absorption spectra of CO, CO<sub>2</sub>, and C<sub>3</sub>H<sub>8</sub>. Upon award, however, we learned that the lasers we intended to use were no longer manufactured and that in order to achieve the appropriate spectral coverage for these species we would have to purchase additional lasers. As a result, we were forced to re-evaluate our plans. We concluded that a Fourier Transform Infrared Spectrometer (FTIR) would be able to collect the appropriate high-resolution absorption spectra of CO, CO<sub>2</sub>, and C<sub>3</sub>H<sub>8</sub> and re-focused the diagnostic aspect of this project accordingly.

#### 3.3.2 Combustion Facility

The combustion facility originally proposed was a parallel plate reactor in which it would be possible to control the wall temperature (and hence heat flux) and thereby investigate the effect of fluid-structure coupling on the combustion processes occurring in a micro-channel. Mid-way through the project, however, we became concerned about two things: First, we felt that our understanding of the flame broadening process was not good enough to ensure that we could build a reactor that could demonstrate the phenomenon properly. Second, we felt that more work than was initially anticipated would be required to get the diagnostic technique to work. As a result, the decision was made to construct a simpler and much less expensive reactor and re-direct some resources

to improving the modeling and proving the diagnostic technique. Nevertheless, a significant amount of work was performed to design the reactor and this is described below.

### 3.4 Original parallel plate reactor design

#### 3.4.1 Original Design

Figure 18 shows the overall design of the parallel plate flow reactor. The test section is formed by two parallel plates that are 120 mm long (in the flow direction) and 70 mm wide. Two quartz or silicon windows form the other two sides of the test section and permit optical access to the reacting flow in the visible or the infrared. The spacing of these plates is adjustable from 0.5 mm to 5 mm to accommodate a range of passage sizes. The plates are supported at each end by temperature-controlled mounts that are equipped with both heating and cooling devices. The outer surface of the plates will be covered with insulating material to limit heat losses to the environment. A large plenum upstream of the test section conditions the flow before it enters the test section and allows time for thorough mixing of the fuel and air prior to entering the test section. Figure 19 is a perspective view of the reactor illustrating the input of reactants, the flow path, and the optical interrogation path.

#### 3.4.2 Flow Regimes Accessible in Original Design

Figure 20 shows contours of Reynolds number as a function of plate spacing and flow rate in the parallel plate flow facility for a channel aspect ratio (width/height) of 10. The dotted box shows the range over which the flow rate and plate spacing can be varied. Note that the top and right boundaries are easily extensible by adding additional flow

metering equipment and enlarging the test section respectively. The figure shows that Reynolds numbers from 0.1 to almost 10000 are accessible in the facility.

The heat transfer coefficient in the rig has also been estimated. The results are summarized in figure 21 which shows the heat transfer coefficient as a function of plate spacing for several Reynolds numbers and plate lengths. The aspect ratio lambda (width/height) is fixed at 10 in this plot but can also be decreased to 1 in the experiment if necessary to provide the appropriate heat transfer coefficient. Note that the heat transfer coefficient is computed using the Nusselt number  $Nu$

$$Nu = \frac{h_c L}{k} \quad (27)$$

and a correlation for entrance flows in channels of rectangular cross-section [38]

$$Nu = Nu_{FD} + \frac{0.03 \left( \frac{D_h}{L} \right) Re_{D_h} Pr}{1 + 0.016 \left[ \left( \frac{D_h}{L} \right) Re_{D_h} Pr \right]^{2/3}} \quad (28)$$

where  $Nu_{FD}$  is the Nusselt number for fully developed flow,  $D_h$  is the hydraulic diameter,  $L$  is the length of the flow passage,  $Re_{D_h}$  is the Reynolds number based on the hydraulic diameter, and  $Pr$  is the Prandtl number.

### 3.4.3 Wall Thermal Conductivity Control

Since one of the objectives of this work is to study the effect of heat conduction in the combustor structure on the reaction zone thickness and the reaction rate, one needs to be able to create combustor walls with a range of thermal conductivities. This is accomplished by creating a composite structure consisting of a layer of Silicon Carbide deposited on stainless steel or Kovar substrates as shown in figure 22. Since the thermal

conductivity of Silicon Carbide is much larger than that of Kovar or Stainless steel, varying ratio of the thickness of the Silicon Carbide layer to that of the substrate allows one to create a variety of structures with overall thermal conductivities that span the range between Silicon Carbide and that of the substrate. Since the thermal conductivity of Silicon Carbide is relatively high (~490 W/mK) and that of Stainless Steel and/or Kovar is relatively low (~15 W/mK), a relatively wide range of structural thermal conductivities can be simulated.

Assuming that the conduction in the side walls is steady and one-dimensional along its length, the thermal resistance of the composite structure can be modeled as two thermal resistances in parallel with one resistance associated with the Silicon Carbide layer and one with the substrate (see figures 22 and 23). The effective thermal resistance of the composite structure is:

$$\frac{1}{R_{eff}} = \frac{1}{R_{SiC}} + \frac{1}{R_{sub}} \quad (29)$$

where the thermal resistance of each component is related to its length  $L_i$ , cross-sectional area  $A_i$  and thermal conductivity  $k_i$  as follows:

$$R_i = \frac{L}{k_i \cdot A_i} \quad (30)$$

Solving for the effective thermal conductivity in terms of the ratio of the thickness of the SiC layer to that of the substrate gives:

$$k_{eff} = \frac{k_{SiC} \frac{h_{SiC}}{h_{sub}} + k_{sub}}{\frac{h_{SiC}}{h_{sub}} + 1} \quad (31)$$

Plotting equation 31 as a function of  $h_{SiC}/h_{sub}$  (figure 24) shows the range of thermal conductivities that could be made available. An additional advantage of using this hybrid structure is that it enables one to vary the thermal conductivity of the structure without varying the chemistry of the surface in contact with the reacting flow. This should enable us to de-couple the effects of varying thermal conductivity of the structure and passage height from the chemistry of the surface.

#### 3.4.4 Wall Temperature Control

Figure 25 is a schematic diagram illustrating the concept behind the temperature controlled supports for the combustor walls. Heat is added to the support using cartridge heaters and is removed from the support using water flow through a water jacket. The mount is be made of copper whose high thermal conductivity minimizes temperature gradients in the mount and to ensure that it remains at a uniform temperature. A detailed energetic analysis of the reactor was performed in order to estimate how much heating and cooling would be required of the actuators. To ensure that the actuators would have adequate authority, all estimates were based on ‘worst case’ scenarios. Three situations were considered: heat loss from the plates to the external environment, heat transfer from the heaters to the flow between the parallel plates (heating requirement), and heat transfer from the reacting flow to the plates (cooling requirement). Figure 26 is a schematic diagram of one of the temperature controlled supports illustrating the flow of coolant.

The ‘worst case’ estimate for losses to the environment corresponds to the situation where the plate is not insulated and the emissivity of the plate is 1.0. Two heat loss

mechanisms are considered: Natural convection and radiation: The correlations in Watts/m<sup>2</sup> are [29]:

- Natural convection

$$\dot{Q}_{NC} = 0.6 \cdot \frac{(T_p - T_e)^{1.25}}{(T_p + T_e)^{2.5}} \quad (32)$$

- Radiation

$$\dot{Q}_R = 10^{-12} \cdot (T_p - T_e)^4 \quad (33)$$

where  $T_p$  and  $T_e$  are respectively the plate and environmental temperature. In this work we assume  $T_e = 300$  K. Figure 27 shows that the worst-case loss for an un-insulated plate at maximum operating temperature could be no more than 1400 W. Adding insulation should drop this loss by at least a factor of two.

The ‘worst case’ design requirement for the heaters is that they must be capable of raising the temperature of the incoming flow to the maximum plate temperature of 1000 K. The power required was estimated using a simple one-dimensional model. The control volume used for the performing the energy balance is illustrated in figure 28 and the governing equation is:

$$\dot{m} \cdot C_p \cdot T(x) - 2 \cdot h_c \cdot (T(x) - T_p) = T(x + dx) \quad (34)$$

$$T(x) = T_p - (T_p - T_0) \cdot \exp\left(-\frac{2 \cdot h_c \cdot W \cdot x}{\dot{m} \cdot C_p}\right) \quad (35)$$

where  $T$  is the fluid temperature,  $T_p$  is the plates ‘temperature’,  $T_0$  is the inlet temperature,  $h_c$  is the convective heat transfer coefficient inside the channel,  $W$  is the width of the plates,  $x$  is the distance from the inlet measured downstream,  $\dot{m}$  is the air flow inside the channel and  $C_p$  is the specific heat at constant pressure for air. Equation 35 is

integrated to determine the temperature profile as a function of downstream distance.

The total heat transferred at the reactor discharge exit ( $x=L$ ) is:

$$P = (T_p - T_0) \cdot \dot{m} \cdot C_p \cdot \left( 1 - \exp \left( -\frac{2 \cdot h_c \cdot W \cdot L}{\dot{m} \cdot C_p} \right) \right) \quad (36)$$

This power depends on the flow rate inside the channel through the heat transfer coefficient  $h_c$ . Since micro-scale heat transfer is still an emerging area of research the Nusselt number was approximated using relations applicable at conventional scales. Table 2 shows the Nusselt numbers, heat transfer coefficients and the estimated heat transfer to the reactor for a range of passage heights at maximum flow rate and the maximum plate temperature of 1000 K.

The ‘worst case’ assumption used to size the cooling elements is that the cooling system would need to be capable of removing all of the heat generated by combustion. Equation 37 describes the energy balance for the system

$$\dot{m}_{mix} \cdot Q_R = \dot{m}_{coolant} \cdot C_{p_{coolant}} \cdot (T_{outlet} - T_{inlet}) \quad (37)$$

where  $Q_R$  is the heat liberated by combustion per unit mass of fuel,  $\dot{m}_{coolant}$  is the flow rate of coolant in the plates ‘temperature control device’,  $C_{p_{coolant}}$  is the specific heat at constant pressure of the coolant,  $T_{outlet}$  is the outlet coolant temperature (about 80C) and  $T_{inlet}$  is the inlet coolant temperature (about 20C). This coolant will probably be chosen as mixed water and glycerol in order to improve the cooling capacity of the device. Figure 29 is a plot showing the minimum flow rate of coolant necessary to absorb all the heat generated by combustion inside the channel. Note, however that because we have used a simple energy balance to determine the coolant flow rate without considering the effectiveness of the heat exchanger, this represents a minimum coolant flow rate.

However, we also recognize that in ordinary operation, we would never want the heat exchanger to remove all (or even half probably) of the heat generated by the flame. Since these effects act in opposition, this simple model presented in equation 37 ought to provide a reasonable estimate of the required coolant flow rate.

### 3.5 Experimental Apparatus

Figure 30 is a schematic diagram of the experimental apparatus used for the ‘proof-of-concept’ experiments. It consists of a BioRad FTS-4000 Excalibur FTIR and a micro-combustor. Figure 31 is a photograph of the silicon-walled micro-combustor with its silicon components removed. Clearly, most of the micro-combustor structure is fabricated of stainless steel. It consists of a small plenum approximately  $9\text{ cm}^3$  in volume where fuel and air are premixed. This discharges into an array of 21 stainless steel tubes, each 20 mm long with an outer diameter of 2 mm and an inner diameter of 1 mm to form a ‘sheet’ of pre-mixed fuel and air. The tube array is sandwiched between two silicon plates, which are mounted separately from the burner, to form a combustion cavity. Finally, two longer tubes with the same diameter are placed at each end of the array to confine the flow of reactants between the silicon plates and to serve as spacers for the silicon plates. Since it is difficult to stabilize a flame at minimum chamber width (ie. when the plates are in direct contact with the tubes and spacers), the burner is operated with the plates spaced 4 mm apart. This allows entrainment of additional air from the room and results in a sheet-like flame stabilized on the end of the tubes in the array. The total volume flow rate through the tubes is  $834\text{ cm}^3/\text{min}$  for the premixed propane / air mixture and corresponds to an average tube discharge velocity of approximately 4.5 cm/s.

The plenum can be translated up and down between the silicon plates using a vertical translation stage.

Figure 32 shows the silicon-walled micro-combustor mounted in the FTIR sample compartment. The FTIR beam passes with normal incidence through the wafers and the focused interrogation region is centered in the high temperature region between the wafers. An aluminum mask with a 4 mm x 8 mm slit defines the interrogation region. The silicon-walled micro-combustor is mounted on a vertical traverse so that the flow can be interrogated over a range of streamwise positions. Figure 33 is an image showing the flame stabilized between the silicon walls. Note that the flame is split and seems to be anchored on both the left and right walls. Spectra are collected at  $0.5 \text{ cm}^{-1}$  resolution, with 20 scans co-added using a linearized, liquid nitrogen cooled. mercury-cadmium-telluride (MCT) detector. The data transfer rate of 10 kHz allows each spectrum to be acquired in approximately 2 minutes.

### 3.6 Experimental Methods

An ambient background scan is acquired before collection of flame data. Dividing the sample spectra by the background spectrum yields a properly normalized transmittance from which species concentration and temperature can be computed. The absorption of silicon is found to be a weak function of temperature; the absorbance of cold versus hot silicon ratioed to an air background is shown in Figure 34. To obtain the spectrum in Figure 35, the combustor was run for several minutes with the silicon plates in position. Once the temperature of the plates reached steady state, the combustor was turned off and a background scan was taken. Air flow continued during this process to ensure that no combustion products remained in the combustor. While the silicon temperature

decreased during the measurement, the scans corresponding to hot and ambient temperature silicon indicate that the difference in transmissivity is relatively small in the  $400 - 4000 \text{ cm}^{-1}$  region. Thus, the temperature dependence of the silicon wafer's transmissivity will not induce significant changes in the background absorption spectrum.

Calibration spectra for CO, CO<sub>2</sub> and C<sub>3</sub>H<sub>8</sub> are obtained at room temperature using a 0.5-liter sample cell with a 3 m path length. The sample cell is evacuated and a known partial pressure of sample gas is introduced. A least squares fit to measurements made at 4 or 5 concentration levels is used to establish the variation of the spectrum with concentration. This is found to be linear.

The Beer-Lambert law describes the relationship between the absorbed signal and concentration:

$$\frac{dI(\bar{v})}{I_0(\bar{v})} = -k(\bar{v}) \cdot C \cdot dx \quad (38)$$

where  $I_0$  is the initial light intensity,  $dI$  is the measured change in transmitted intensity due to the absorbing sample,  $\bar{v}$  is optical frequency (typically in  $\text{cm}^{-1}$  for infrared measurements),  $C$  is the concentration,  $dx$  is the differential pathlength, and  $k$  is an absorption coefficient that accounts for the variation of absorption with wavelength. Integrating over the optical path length and converting natural logarithms to base 10 gives:

$$\log_{10} \frac{I(\bar{v})}{I_0(\bar{v})} = A(\bar{v}) = \epsilon(\bar{v})CL \quad (39)$$

Here  $A$  is the absorbance,  $L$  is the path length, and  $\epsilon$  is the molar absorptivity that is a function of optical frequency. Further, for each molecule the wavelength-integrated absorbance  $\bar{A} = \int \epsilon(\bar{v})CLd\bar{v} = \bar{\epsilon}CL$  can be determined by summing the absorbance over

all lines in the ro-vibrational band. Treating  $\bar{\epsilon}$  as a constant results in the following expression that can be used to deduce the concentration from measurements of  $\bar{A}$  in the sample and calibration cell

$$C_{sample} = \frac{\bar{A}_{sample}}{\bar{A}_{calibration}} \cdot C_{calibration} \cdot r_{path} \quad (40)$$

where  $r_{path}$  is the ratio of the pathlengths ( $L_{calibration}/L_{path}$ ) for the sample and calibration. The error introduced by using equation 40 is small because  $\bar{\epsilon}$  a relatively weak function of temperature and the vibrational populations of the molecules being studied are relatively weakly perturbed (ie. by no more than 15% of their room temperature values). Note that vibrational population corrections could also be implemented relatively easily, but were deemed unnecessary for these preliminary measurements.

The populations of the various rotational bands do change significantly with temperature and this property was used to infer gas temperature from CO spectra recorded by the FTIR. An algorithm was developed that matches a standard temperature-dependent rigid-rotor model of the CO  $\Delta v = 0 \rightarrow 1$  ro-vibrational absorption spectra to the actual data. The wavelengths for the spectral lines are given by the following equation in which ‘ describes the upper state and “ describes the lower state [39]:

$$\bar{\nu} = \bar{\nu}_0 + B'_v J'(J'+1) - D'_v J'^2 (J'+1)^2 - B''_v J'' (J''+1) + D''_v J''^2 (J''+1)^2 \quad (41)$$

Here  $J$  is the rotational level,  $\bar{\nu}$  is the wavenumber of a particular ro-vibrational transition,  $\bar{\nu}_0$  is the central wavenumber of the band, and  $B_v$  is the rotational constant described by

$$B_v = B_e - \alpha_e (\bar{\nu} + \frac{1}{2}) \quad (42)$$

where  $\alpha_e$  is the vibration-rotation coupling constant.  $D_v$  is the centrifugal distortion constant described by

$$D_v = D_e - \beta_e (\bar{v} + \frac{1}{2}) \quad (43)$$

Since  $\beta_e$  is small compared to  $D_e$ , it is ignored in the analysis. Boltzmann statistics give the relative fraction of molecules in each rotational state:

$$f_J = (J' + J'' + 1) e^{-[hc(J'(J'+1)B_v + J''^2(J'+1)^2D_v)]/kT} \quad (44)$$

In equation (33)  $h$  is Planck's constant,  $c$  is the speed of light, and  $k$  is Boltzmann's constant. The pre-exponential term is modified from the familiar degeneracy  $(2J' + 1)$  to include variation in the dipole moment and transition probability as described in Herzberg [38]. Knowing both the position of each peak and the relative fraction of molecules contained therein as a function of temperature, enables one to develop an analytical expression for the spectrum as a function of temperature that may be fit to the experimental data.

The individual peak heights are determined from the experimental data by finding the highest measured point at the wavenumber of each peak, and subtracting a spectral baseline calculated from the minima between the peaks. The resulting experimental peak heights are then normalized and matched to the relative fraction of molecules in equation 33 using a nonlinear least squares fit, yielding the temperature.

### 3.7 Results and Discussion

Measurements were made in the combustor at points visually located between 0 and 12 mm downstream of the flame front. While every effort was made to stabilize premixed flames at a variety of equivalence ratios, the stability limits of the burner were

very narrow and entrainment of air from the sides and bottom was required to obtain a stable flame. This resulted in a partially premixed flame which we assume burns with an overall equivalence ratio of unity.

Figure 35 is a typical spectrum showing features of CO and CO<sub>2</sub>. The P and R branches of CO are easily observed in the wavelength region from 2000 – 2300 cm<sup>-1</sup> while CO<sub>2</sub> is observed in the range 2100 – 2500 cm<sup>-1</sup>. Noise in the spectrum is apparent and arises from flame fluctuations and aliasing resulting from the limited bandwidth of the measurement. While the spectrometer is capable of 0.1 cm<sup>-1</sup> resolution under normal conditions, the low, fluctuating light level prevented measurements at any resolution lower than 0.5 cm<sup>-1</sup>. The noise makes it difficult to resolve peak heights associated with the higher rotational levels.

Temperature is determined by fitting the CO model to the experimental data. Peaks are located using eq. 41, in which the actual maximum from the data in the immediate vicinity of the expected peak is found, and the baseline is determined by finding the minimum points between the peaks. Figure 36 shows a typical spectrum, taken at room temperature in a 10-meter cell where the peaks have been identified. The locations and relative amplitudes of these peaks are tabulated and compared to the known line locations and the relative amplitudes predicted by equation 41. The temperature is determined using a non-linear least squares method to minimize the difference between the measured and predicted line amplitudes.

Figure 37 compares the relative amplitudes of the peaks of the room temperature sample in Figure 36 to those corresponding to the best fit. The temperature corresponding to the best fit ( $R^2 = 0.88$ ) was 388K - somewhat higher than room

temperature, which may be an indication of the magnitude of the error induced by the undersampling. Undersampling, due to the fact that our spectral resolution was relatively coarse ( $0.5 \text{ cm}^{-1}$ ) compared to the broadened line widths of 0.1 to  $0.2 \text{ cm}^{-1}$ , causes the some of the peak heights to be underreported. Another possible source of error is interference from higher order absorptions (e.g. absorptions corresponding to  $\Delta\nu = 1 \rightarrow 2$ ) which weakly overlays the CO spectrum, particularly the P branch.

Figure 38 illustrates the measured and predicted line intensities for a high temperature spectrum taken 9 mm downstream of the visible flame. The theoretical best fit to the experimental data shown in the figure is 829 K. The high-temperature spectrum is much noisier than the low temperature spectrum, thus the correlation between the measured and predicted line amplitudes is much lower. Other important sources of noise include flame and flow fluctuations, and the fact that the temperature, and therefore the rotational level populations, probably vary along the beam path.

Figure 39 depicts the best-fit gas temperature as a function of downstream distance in the microburner. The error  $\delta_T$  shown in the figure is calculated based on the RMS noise in the measurement, the residual of the fit between the experimental and theoretical spectra, and the error in the population equation (44) due to temperature.

$$\delta_T = (v_{\text{residual}} + \sigma_{\text{rms}}^2) \cdot \left( \frac{\partial f}{\partial T} \right) \quad (45)$$

where  $v_{\text{residual}}$  is the standard deviation of the residual from the nonlinear least squares fit,  $\sigma_{\text{rms}}$  is the root mean square noise of the sample and  $\partial T$  the partial derivative of equation 44 with respect to temperature. The temperature has the proper qualitative behavior showing a decrease in temperature in the post-flame as the gases lose heat to the environment. The first two data points at 0 mm and 1 mm had an  $R^2$  value of less than

0.3, and hence are included only for reference and are presented without error bars as the actual error in the flame zone is quite high due to fluctuations.

Figure 40 shows the relative concentration of fuel ( $C_3H_8$ ) and  $CO_2$  as a function of downstream distance. As indicated earlier, concentration can be determined from the area under the peaks and equation 40. Uncertainties in the pathlength and low signal levels prevented absolute quantification. Rotational lines were not resolved at the 0.5  $cm^{-1}$  resolution of the measurement and the propane signal was almost in the noise, further limiting the accuracy of the measurement. However, as observed, relative  $CO_2$  and  $C_3H_8$  concentrations appear to be roughly constant in the cooling post-flame region, as expected.

### 3.8 Conclusions of Proof-of-Concept Experiments

This work illustrates the potential for making infrared measurements of species concentration and temperature in microscale systems by imaging through crystalline silicon walls. The technique has been demonstrated in the post-flame region of a micro-burner. With further improvements it could be very useful in assessing combustion completeness and the extent of flame / structure interaction in MEMS-based combustion systems. Furthermore, this work has also shown that other IR techniques like tunable diode laser absorption spectroscopy could be used to make high-speed non-intrusive measurements in silicon MEMS combustion systems.

### 3.9 Improved Experimental Apparatus

Figures 41 and 42 show the improved experimental apparatus presently being used to develop the non-intrusive diagnostic technique. It consists of a more versatile micro-burner and a Nicolet Nexus 870 Fourier Transform Infrared Spectrometer. This instrument is an order of magnitude more sensitive than the one used to demonstrate the measurement concept and also has better spectral resolution ( $0.5\text{ cm}^{-1}$ ). This makes it much easier to acquire well-resolved rotational spectra. The instrument has the additional advantage of being able to stop its scanning mirror at particular wavelengths which makes it useful for future work involving hyperspectral imaging.

Unlike the ‘proof of concept’ experiment in which the combustor was located in the sample compartment, now the combustor is located on the optical table adjacent to the FTIR. A pair of 90 degree parabolic mirrors directs the interrogation beam outside the FTIR, through the burner, and onto the FTIR’s detector which has been removed from the instrument chassis and attached to the optical table. The first parabolic mirror has a focal length of 203mm and reduces the beam diameter from about 38 mm to 10 mm. The burner is placed at the focal point and a horizontal slit cut in a piece of shim stock is placed immediately in front of the combustor to improve the spatial resolution of the measurement to 1 mm in the flow direction. The second parabolic mirror has a focal length 50.8mm and directs the transmitted beam onto the detector. The burner is supported by an adjustable jack. Raising or lowering the jack traverses the interrogation volume in the flow direction making it possible to collect spectra (and thereby measure species concentration and temperature) as a function of streamwise position in the flame.

Figure 43 is a drawing of the ‘second generation’ micro-burner showing the various critical components. Pre-mixed fuel and air are introduced into the plenum and pass vertically upward between two silicon wafers. Two vertical guides support the wafers on the outside and a set of 4 vertically-oriented stainless-steel tubes (two at each wafer edge) support the wafers from the inside. The diameter of the tubes fixes the minimum wafer spacing and the burner is always operated at the minimum spacing with both wafers in contact with the tubes. This can be seen more clearly in figure 44 which is a top view.

### 3.10 Challenges

One major challenge involved leaks in the micro-burner. Room air was being entrained between the plates diluting the mixture and making it impossible to obtain reliable concentration measurements. After a lot of experimentation, a pair of ‘C’ shaped baffles were constructed and slid over the edges of the silicon wafers. The interior of the ‘C’ was packed with glass wool and this seems to have successfully blocked entrainment from the environment. Figure 45 shows several spectra of CO<sub>2</sub> acquired in the second-generation micro-burner with the ‘C’ shaped baffles. They indicate that repeatability is very good.

Another major challenge involved the interpretation of the spectra to determine temperature. Temperature in the proof-of-concept experiments was determined based on the rotational structure of the CO band as discussed in section 3.6. However, the repeatability of the measurements, even with the new spectrometer, was not good. There were two reasons for this. First, it remained difficult to adequately resolve the peaks in the rotational spectra and second, the models for the temperature dependence of the

rotational structure of CO did not work well at high (combustion) temperatures. After some investigation, we discovered that temperature measurement techniques based on the vibrational bands of CO<sub>2</sub> are more reliable at high temperatures [40] and we are in the process of switching over to this method for measuring gas temperature. The general procedure for fitting the recorded spectra to the band model is the same as in the proof-of-concept experiments, but now we use vibrational spectra and a band model based on the EM2C data base [41] which is more reliable at combustion temperatures.

### 3.11 Results

Figure 46 shows preliminary measurements of temperature as a function of downstream distance in the second-generation micro-burner. The stars correspond to gas temperatures computed from vibrational spectra of CO<sub>2</sub>, and the crosses correspond to the uncorrected output of a K-type thermocouple traversed in the streamwise direction through the flame. Each data point corresponds to an average of 100 spectra over the 800 to 4000 cm<sup>-1</sup> range. The approximately 70 K difference between the spectroscopic and thermocouple measurements is probably due to the fact that the thermocouple measurements are un-corrected for the effects of radiation and conduction losses. The vibrational band model is less effective at low temperatures and this results in increased scatter in the data at large downstream distances where the products have cooled significantly.

### 3.11 Future Work

Work on the interpretation of the vibrational spectra continues and the results of the previous section suggest that a hybrid approach that uses vibrational spectra for temperature measurements in high temperature regions and rotational spectra for measurements in low temperature regions may be most appropriate. Work continues to improve the optical assembly used to reduce the FTIR beam diameter. The objective is to reduce the beam size as much as possible before it encounters the mask so that as much energy as possible passes through the sample. This may best be accomplished by using a pair of high temperature optical fibers to deliver light to and from the interrogation region. Finally, once the diagnostic technique is better developed, a more sophisticated parallel plate reactor with wall temperature control will be constructed.

## 4.0 Overall Conclusions

The thermal coupling between a chemically reacting gas stream and the thermally conductive structure that contains it has been investigated analytically and computationally. Understanding the physics of combustion in micro-channels is important for the development of compact and highly scalable propulsion systems for the fleet of micro, nano, and pico-satellites envisioned by the US Air Force.

The results of the present investigation indicate that heat exchange between the gas and structure has very important effects on the structure and propagation of the flame. In addition to the well-known phenomenon of thermal quenching, heat exchange has been shown to broaden the reaction zone and increase the reaction rate. The passage height,

the Nusselt number, and the thermal conductance of the structure are the primary parameters that determine the length scale at which the transition from gas-dominated to structure-dominated combustion occurs. Since the increase in reaction rate is larger than the magnitude of the flame broadening, it is possible to find combinations of passage height and length where power density is maximized. The chemistry of the fuel also appears to influence the optimum combustor design and leads to two optimum configurations for a CH<sub>4</sub>-air combustor but only one optimum configuration for a H<sub>2</sub>-air combustor.

A non-intrusive diagnostic technique for making measurements in these micro-flows has also been demonstrated. While more work is necessary to refine the technique, measurements of temperature and species concentration with adequate spatial resolution for verifying model predictions were demonstrated. A special parallel plate flow reactor with walls whose temperature can be controlled was designed, but was not constructed. Instead, two simpler burners were constructed for the purposes of demonstrating the diagnostic technique. Eventually, the diagnostic technique will be applied in the more sophisticated parallel plate facility.

Other important outcomes of this research program include the following:

- 1 graduate student fully supported
- 20% support for a second graduate student
- 3 journal articles submitted
- 4 conference papers
- 6 conference presentations
- 1..5 MS theses completed

- 50% of a PhD thesis completed

## 5.0 Publications

### 5.1 Journal Articles

1. Heatwole, S., Cadou, C. P., and Buckley, S. G., "In situ Infrared Diagnostics in a Silicon-Walled Microscale Combustion Reactor: Initial Measurements", submitted to *Combustion Science and Technology*
2. Leach, T., Cadou, C. P., and Jackson, G., "Effect of Structural Heat Conduction and Heat Loss on Combustion in Micro-channels", submitted to *Combustion Theory and Modeling*
3. Leach, T., Cadou, C. P., "The Role of Structural Heat Exchange and Heat Loss in the Design of Efficient Silicon Micro-combustors", submitted to the 30<sup>th</sup> *International Symposium on Combustion*

### 5.2 Conference Papers and Presentations

1. Leach, T., Cadou, C. P., and Jackson, G., "Numerical Simulation of the Micro-combustion Between Two Parallel Plates", 3rd Joint Meeting of the US Sections of the Combustion Institute, Chicago, IL, March 17-19, 2003
2. Cadou, C. P., "Reactive Processes in Micro-scale Combustion Systems", Invited talk, Western States Section of the Combustion Institute, October 20-21, Los Angeles, CA 2003
3. Heatwole, S., Cadou, C. P., Buckley, S. G., "In-situ FTIR Measurements in a Micro-scale Combustion Reactor", Western States Section of the Combustion Institute, October 20-21, Los Angeles, CA 2003
4. Leach, T. T., and Cadou, C. P., "Modeling and Simulation of Fluid-Structure Coupling in Micro-combustors", 42nd AIAA Aerospace Sciences Meeting and Exhibit, Reno NV, January 5-8, 2004
5. Heatwole, S., Buckley, S., and Cadou, C. "MEMS Alliance Symposium, Johns Hopkins Applied Physics Laboratory, March 29-30, 2004
6. Leach, T. and Cadou, C. "Effect of Structural Heat Conduction on Flame Propagation and Power Density in Micro-Combustors", MEMS Alliance Symposium, Johns Hopkins Applied Physics Laboratory, March 29-30, 2004

## 6.0 Executive Summaries of Theses

### 6.1 Timothy Leach

Modeling and Simulation of the Microcombustion Between Two Parallel Plates.

Master of Science Thesis

June, 2003

University of Maryland, Department of Aerospace Engineering  
College Park MD, 20816

#### Introduction

The interest in building smaller satellites weighing between 0.1 kg and 10 kg has fostered a great concentration on micro-propulsion systems. In particular, chemical fuels are an attractive option because of their high energy density. However, existing chemical micro-propulsion devices are very inefficient. While this can be partly attributed to greater heat loss to the environment, another important phenomenon that occurs at microscale is reaction zone broadening. This arises from the enhanced thermal coupling between the reacting gas and the structure of the micro-combustor and degrades the chemical efficiency of the combustor. The objective of this thesis is to understand the basic physics of this thermal coupling and to study the effect of certain parameters on the resulting flame broadening. This is done by developing an analytical model and a numerical simulation.

#### Analytical model

The model uses reasoning similar to that employed in the thermal theory of Mallard and Le Chatelier. While this theory states that flame propagation is the result of a thermal balance between conduction and convection in the gas, the additional effect of conduction within the structure is added. Figure 1 shows the schematic diagram of the problem considered and the different fluxes involved. Note that the computational grid shown in the figure is used in the second part of this work.

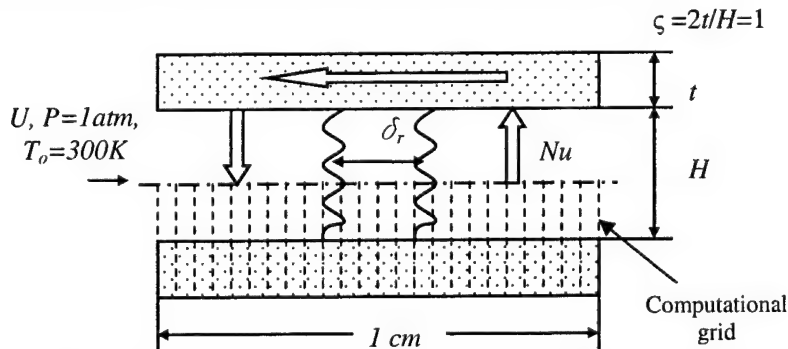


Figure 1: Schematic diagram of the problem studied showing the different fluxes

Figure 2 presents the thermo-electrical analogy for this problem that is used to solve for the reaction zone thickness  $\delta_r$  by performing a thermal balance between the post-flame region and the pre-flame region. The analysis of the problem leads to the following expression for the reaction zone thickness:

$$\delta_r = \sqrt{\beta} \sqrt{\frac{k_r}{\rho C_p} \frac{T_f - T_i}{T_i - T_0} \frac{1}{RR}} = \sqrt{\beta} \delta_{r,fr} \quad (1)$$

where

$$\beta = \frac{1 + \zeta \frac{k_s}{k_r} \left( 1 + \frac{4H}{\delta_r} \frac{1}{Nu} \right)}{1 + 4\zeta \frac{k_s}{k_r} \frac{H}{\delta_r} \frac{1}{Nu}} \quad (2)$$

and  $\delta_{r,fr}$  is the reaction zone thickness of a freely propagating flame.

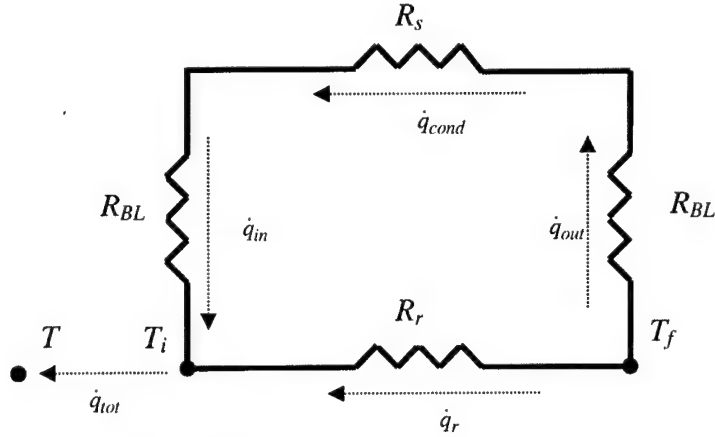


Figure 2: Thermo-electrical analogy for the thermal theory with thermal coupling with the structure

It can be seen that equations 1 and 2 predict a limit cycle behavior of the flame thickness with H:

- As  $H \rightarrow \infty$ ,  $\delta \rightarrow \delta_{r,fr}$  and we recover the freely propagating case.
- As  $H \rightarrow 0$ ,  $\delta_r \rightarrow \sqrt{1 + \frac{k_s}{k_r} \zeta \delta_{r,fr}}$ : the value for the flame thickness is set by the ratio of the thermal conductance of the structure to that of the gas and is always greater than the value associated to a freely propagating flame.

### Numerical simulation

In order to confirm the results predicted by the simple analytical model, a numerical simulation is implemented. The computational domain is shown in figure 1. It involves a one-dimensional mesh on which the continuity, species, and energy equation for both the gas and the structure are solved. The pressure is taken to be constant to 1 atm so that the momentum equation does not need to be solved. In this work, only gas-phase combustion is investigated and surface reactions and in particular catalytic reactions, are not taken into account. A 9-species, 19-reaction chemical mechanism is used to model the H<sub>2</sub>-air combustion. The grid consists of 201 equally spaced points and was checked to be resolved enough to capture the flame accurately. The length of the computational domain is 1 cm and allows for the entire reaction zone to be captured for all cases reported here. The flame thickness is computed based on the gas-phase temperature profile.

### Results and discussion

Figure 3 shows the evolution of the non-dimensional flame thickness as a function of non-dimensional passage height for various values of the Nusselt number and at a specified value of the thermal conductivity of the structure (10 W/m/K). Note that the reference length scale is the flame thickness associated with a freely propagating flame. The figure shows that for  $Nu=0$ , the flame thickness remains constant at a value equal to the freely propagating case. This makes sense since for  $Nu=0$  there is no more coupling between the gas and the structure of the combustor. The figure also shows that the strength of the thermal coupling between the fluid and the structure (determined in part by  $Nu$ ) determines at what  $H$  the transition from gas to structure-dominated heat transfer occurs. Both the analytical model and numerical

simulation yield the same behavior and agree qualitatively. The major discrepancy involves predicting the amplitude of the flame broadening, but this is to be expected from such a simple theory and the good qualitative agreement indicates that the underlying physics appears to be described correctly.

Figure 4 shows the evolution of the non-dimensional flame thickness as a function of non-dimensional passage height for various values of the non dimensional thermal conductivity of the structure and at a specified value of the  $Nu$  ( $Nu=3$ ). Note that the reference thermal conductivity is that of the gas. The figure shows that the thermal conductivity of the structure influences the amplitude of the flame broadening. This makes sense since increasing the thermal conductivity of the structure allows a larger amount of heat to be transferred from the post-flame to the pre-flame through the structure. Once again the analytical model and numerical simulation agree qualitatively with each other but in all cases the analytical model overpredicts the amplitude of the flame broadening.

Many factors contribute to the discrepancy in the amplitude of the broadening predicted by the numerical and analytical models. Some important differences include the use of multi-step versus single step chemistry, variable versus fixed gas-phase properties, and the use of discrete versus distributed heat transfer between the gas and the structure.

The results suggest that building compact efficient micro-combustors can be hard if the thermal coupling between the gas and the structure of the combustor is not taken into account in the design process.

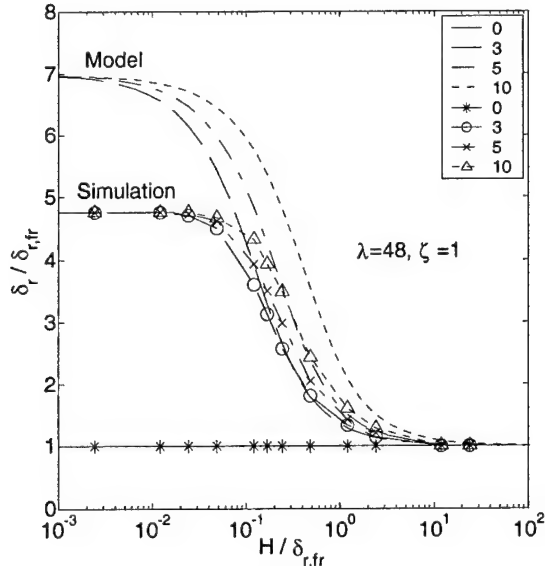


Figure 3: Fractional increase in reaction zone length  $\delta_r$  as a function of the normalized flow passage height  $H/\delta_{r,fr}$  for a range of Nusselt numbers. The solid lines correspond to the analytical model and the symbols correspond to results from the numerical simulations.

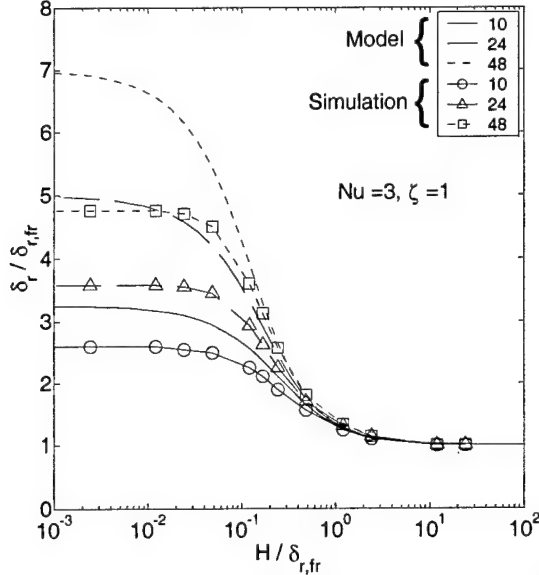


Figure 4: Fractional increase in reaction zone length  $\delta_r$  as a function of the normalized flow passage height  $H/\delta_{r,fr}$  for a range of normalized structure thermal conductivity  $\lambda$ . For the analytical model,  $k_s=0.21$  W/mK. Solid lines correspond to the analytical model and the symbols correspond to numerical model results.

### Conclusion

An analytical model was derived to represent the basic physics of the thermal coupling between a reactive mixture and a thermally conductive structure in order to understand the behavior of flames in micro-combustors. This model indicates that thermal exchange in the structure leads to a broadening in the reaction zone. It also predicts that the onset of the flame broadening depends on the Nusselt number and the passage height while the amplitude of the flame broadening depends on the thermal conductivity of the structure. A more detailed numerical simulation of the combustion of a premixed mixture of  $H_2$  and air provides qualitative confirmation of the trends identified by the analytical model.

These results are important because they suggest that micro-combustors need to be proportionally longer than conventional combustors in order to achieve a good efficiency.

Note: The results presented in this summary do not coincide entirely with those reported in the thesis since a slight mistake was made in the implementation of the numerical code at the time the thesis was written

## 7.0 References

1. Lewis, B. and von Elbe, G., Combustion, Flames and Explosions of Gases, second edition, Academic Press, 1961.
2. Friedman, R., Third Symposium (International) on Combustion, The Combustion Institute, 1949, pp. 110-120.
3. von Karman, Th. and Millan, G., Fourth Symposium (International) on Combustion, The Combustion Institute, 1953, pp. 173-178.
4. Putnam, A. A., Smith, L. R., Fourth Symposium (International) on Combustion, The Combustion Institute, 1953, pp. 708-714.
5. V. V. Zamashchikov, *Combustion Sci. and Tech.* 166 (2001) 1-14
6. Peterson, R. B., 'Size Limits for Regenerative Heat Engines', *Microscale Thermophysical Engineering*, 2, pp 121-131, 1998.
7. Aichlmayr, H. T., Kittelson, D.B., and Zachariah, M. R. 'Modeling HCCI Combustion in Small Scales with Detailed Homogeneous Gas Phase Chemical Kinetics', *Chemical Engineering Science*, v. 57, n. 19, Oct 21 2002, pp. 4161-4171.
8. Daou, J. and Matalon, M., 'Influence of Conductive Heat Losses on the Propagation of Premixed Flames in Channels', *Combustion and Flame* 128 (2002) 321-339.
9. Daou, J. and Matalon, M., 'Flame Propagation in Channels: Differential Diffusion Effects', 3<sup>rd</sup> Joint Meeting of the U.S. Sections of The Combustion Institute, March 2003.
10. Ronney, P.D., 'Analysis of non-adiabatic heat-recirculating combustors', accepted by *Combustion and Flame*, to appear 2004.
11. Mehra, A, 'Development of a High Power Density Combustion System for a Silicon Micro Gas Turbine Engine', Ph.D. Thesis, MIT, Feb 2000.

12. Spadaccini, C. M, Zhang, X., Cadou, C. P., Miki, N., and Waitz, I. A., 'Development of a Catalytic Silicon Microcombustor for Hydrocarbon-fueled Power MEMS', Proceedings of the IEEE Micro Electro Mechanical Systems (MEMS), 2002, p. 228-231.

13. Mallard, E. and Le Chatelier, H. L., Ann. Mines 4 (1883) 379.

14. D. B. Spalding, *Proc. Royal Soc. A*, 240, 1220 (1957) 83-100.

15. Hardesty, D. and Weinberg, F., *Combustion Sci. and Tech.* 8 (1974) 201-214

16. T. Takeno, K. and Sato, K *Combustion Sci. and Tech.* 20 (1979) 73-84

17. Coffee, T.P., Kotlar, A.J., and Miller, M.S., 'The Overall Reaction Concept in Premixed, Laminar, Steady-State Flames. I. Stoichiometries', *Combustion and Flame* 54 (1983) 155-169.

18. Zhu, H. and Jackson, G.S., 'Transient Modeling for Assessing Catalytic Combustor Performance in Small Gas Turbine Applications', 2001-GT-0520, Proceedings of ASME Turbo Expo 2001: 46<sup>th</sup> ASME International Gas Turbine & Aeroengine Technical Congress, New Orleans, LA, June 4-7, 2001.

19. Miller, J. A., and Bowman, C. T., *Progress in Energy and Combustion Science* 15 (1989) 287-338.

20. Deuflhard, P., Harier, E., and Zugck, J., , 'One-step and Extrapolation Methods for Differential-Algebraic Systems', *Numer. Math.* 51 (1987) 501-516.

21. Miller, J.A., Mitchell, R.E., Smooke, M.D., and Kee, R.J., *Proc. Comb. Inst.* 19 (1982) 181.

22. Law, C.K, 'A Compilation of Experimental Data on Laminar Burning Velocities' in: N. Peters and B. Rogg, (Eds) *Reduced Kinetic Mechanisms for Applications in Combustion Systems*, Springer-Verlag, New York, 1993, pp. 15-26

23. Law, C.K. and Sung, C.J., 'Structure, aerodynamics, and geometry of premixed flamelets', *Progress in Energy and Combustion Science* 26 (2000) 459-505.

24. Glassman, I., *Combustion*, Third edition, Academic Press, 1996.

25. Lide, D.R (ed.), *CRC Handbook of Chemistry and Physics*, 81<sup>st</sup> ed.

26. A. Carlos Fernandez-Pello, *Proc. Combust. Inst.* 29 (2002)

27. W. A. Strauss, R. Edse, *Proc. Combust. Inst.* 7 (1959) 377.

28. X. Zhang, A. Mehra, A.A. Ayon, and I.A. Waitz, "Igniters and Temperature Sensors for a Micro-Scale Combustion System," *Sensors and Actuators, A* 103 (1-2) (2003) 253-262.

29. Spitzer, W. and H. Y. Fan, *Phys. Rev.* 108, 2 (1957) 268-271.

30. Schroder, D. K., R. N. Thomos, and J. C. Swartz, *IEEE Trans. Electron. Dev.* ED-25, 2(1978) 254-261

31. Hara, H. and Y. Nishi, *J. Phys. Soc. Jpn* 21, 6 (1966) 1222.

32. Runyan, W. R., *Technology Semiconductor Silicon*, McGraw-Hill Book Company, 1966.

33. Wereley, S. and Meinhart, C., 'Second Order Accurate Particle Image Velocimetry', *Experiments in Fluids*, vol 31, no 3, September 2001

34. Meinhart, C.D., Wereley, S. T., and Santiago, J. G, in *Laser Techniques Applied to Fluid Mechanics*, Adrian, R. J. (ed.), Springer-Verlag, Berlin, pp. 57-70

35. Han, G., Bird, J. C., Westin, J. A., and Breuer, K. S., 'Infrared Diagnostics for Measuring Fluid and Solid Motion Inside MEMS', *Solid-State Sensor and Actuator Workshop*, Hilton Head Island, SC, June 2-6 2002

36 Nakanishi, K., 'Practical Infrared Absorption Spectroscopy', Holden Day, San Francisco, 1962

37 Mihalcea, R. M., Baer, D. S, and Hanson, R. H. Twenty Seventh Symposium (International) on Combustion/ The Combustion Institute, 1998, 95-101

38 Mills, A. Basic Heat and Mass Transfer, pp. 240

39 Herzberg, G. 1950. *Spectra of Diatomic Molecules*, pp. 658 Princeton, NJ, Van Nostrand.

40 Modest, M. F. and Bharadwaj, S. P., JQSRT 73, 2002, pp. 329-338

41 Soufiani, A., and Taine, J. , Int. J Heat Mass Transfer, 23, 1980, pp. 147-157

| Parameter                               | 1 atm               |                     | 5 atm               |                      | 10 atm                |                      |
|---|---------------------|---------------------|---------------------|----------------------|-----------------------|----------------------|
|   | Ad.                 | Non-Ad.             | Ad.                 | Non-Ad.              | Ad.                   | Non-Ad.              |
| $\dot{w}_D / \dot{w}_{D,ref}$           | 64                  | 60                  | 326                 | 323                  | 475                   | 471                  |
| $H/\delta_{r,fr}$                       | <0.002              | 0.01                | <0.012              | 0.006                | <0.1                  | 0.016                |
| $L/\delta_{r,fr}$                       | 1                   | 1                   | 1.31                | 1.31                 | 1.6                   | 1.6                  |
| $U/S_{L,ref}$                           | 5.44                | 5.16                | 4.44                | 4.42                 | 5.06                  | 5.01                 |
| Efficiency (%)                          | 90                  | 89                  | 92                  | 91                   | 96                    | 96                   |
| $\dot{w}_{D,ref}$ (MW/cm <sup>3</sup> ) | 177                 | 177                 | 1230                | 1230                 | 3180                  | 3180                 |
| $\delta_{r,fr}$ (cm)                    | 0.055               | 0.055               | 0.008               | 0.008                | 0.006                 | 0.006                |
| $S_{L,fr}$ (cm/s)                       | 90                  | 90                  | 136                 | 136                  | 187                   | 187                  |
| V (cm <sup>3</sup> /cm)                 | <6x10 <sup>-6</sup> | 30x10 <sup>-6</sup> | <1x10 <sup>-6</sup> | 0.5x10 <sup>-6</sup> | <5.8x10 <sup>-6</sup> | 0.9x10 <sup>-6</sup> |

Table 1: Summary of optimum power density configurations for a silicon micro-combustor. The fuel is H<sub>2</sub> burning in air and the equivalence ratio is 0.5.

| Passage height (mm) | <i>Nu</i> | <i>h<sub>c</sub></i> (W/(m <sup>2</sup> .K)) | <i>P</i> (W) |
|---------------------|-----------|--|--------------|
| 0.5                 | 8.12      | 572  | 50           |
| 1                   | 8.00      | 284  | 100          |
| 2                   | 7.76      | 139  | 150          |
| 5                   | 7.13      | 53   | 300          |

Table 2 Estimated heat transfer coefficients and maximum heat transfer to gas flow

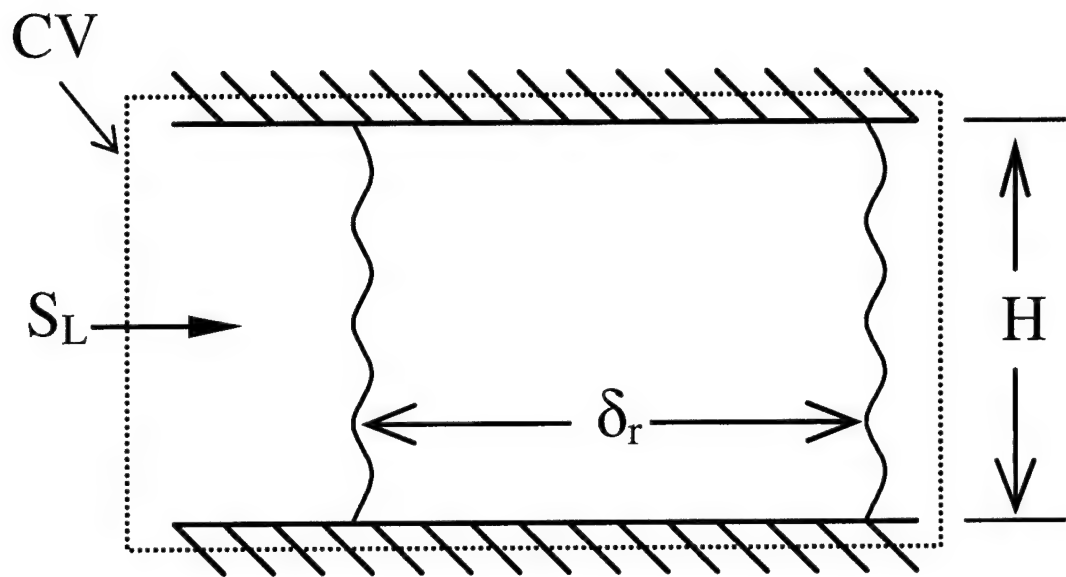


Figure 1: Flame stabilized in a passage where  $H \sim \delta_r$ .

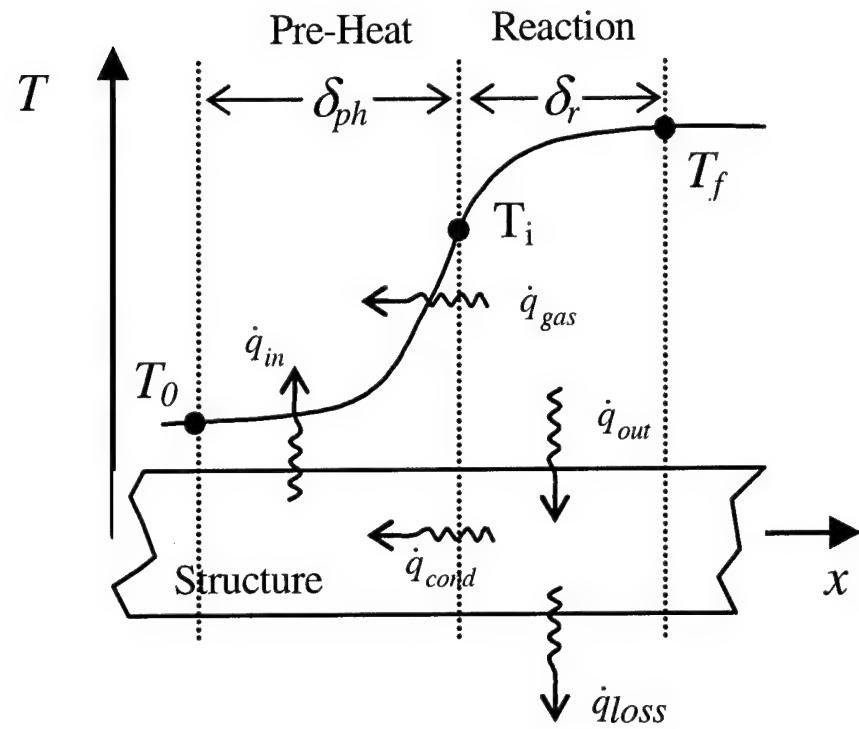


Figure 2: Thermal exchange in a flame in close contact with a structure.

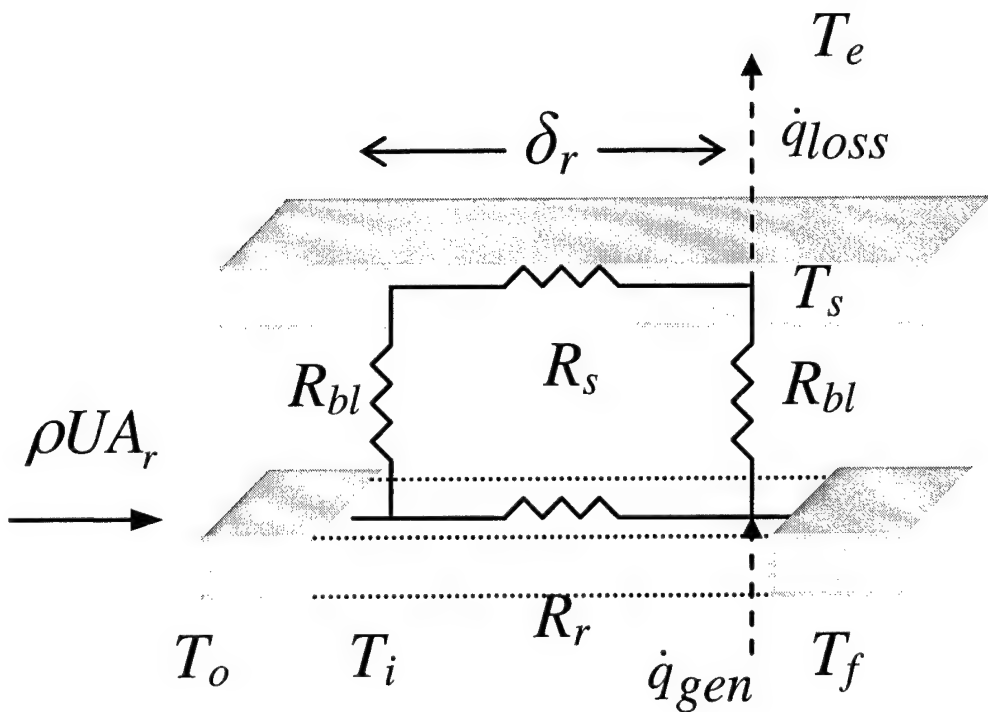


Figure 3: Thermal resistor network for visualizing heat exchange between gas and structure and heat loss to the environment.

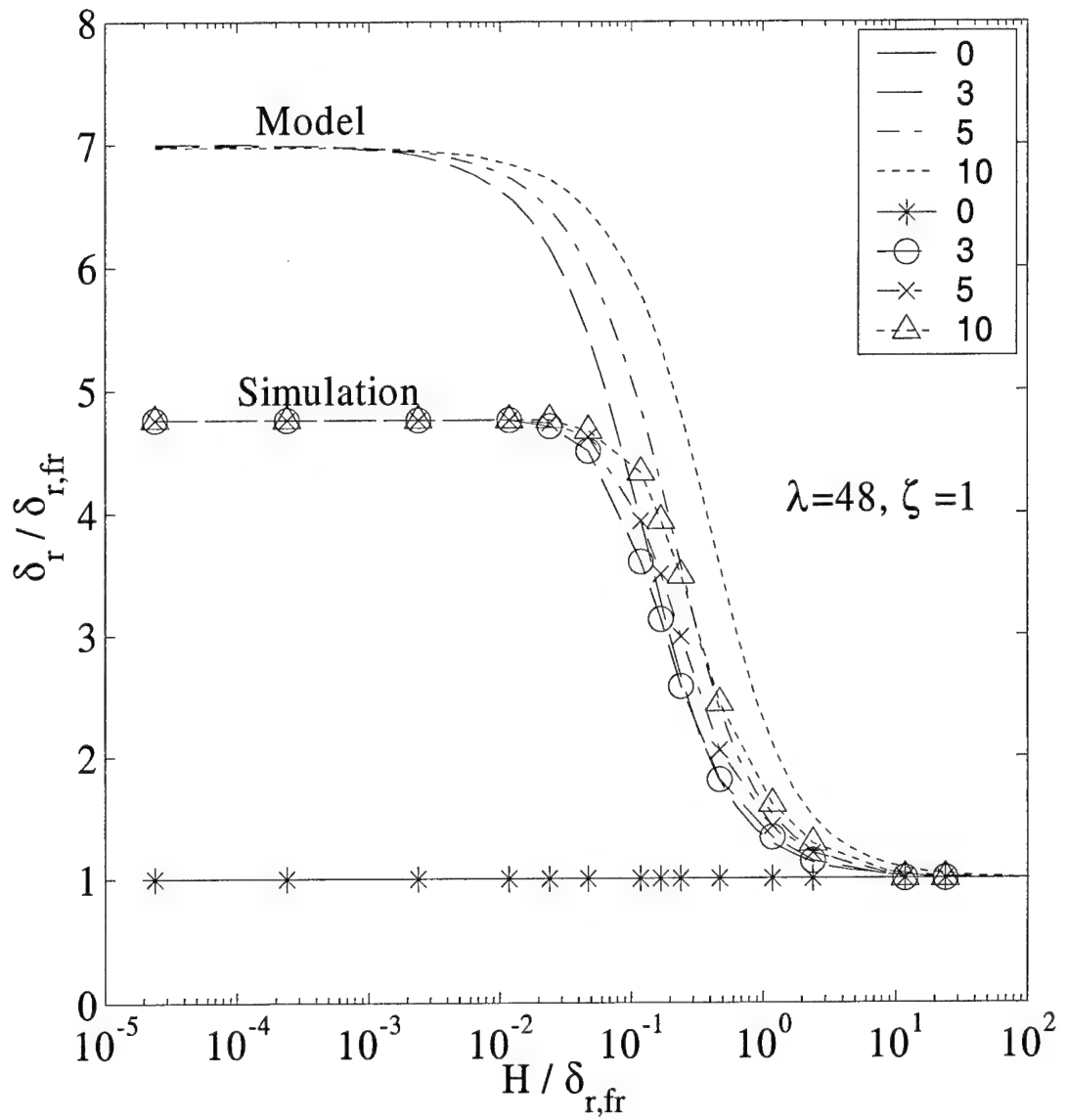


Figure 4: Fractional increase in reaction zone length  $\delta_r$  as a function of the normalized flow passage height  $H/\delta_{r,fr}$  for a range of Nusselt numbers. The solid lines correspond to the analytical model and the symbols correspond to results from the numerical simulations.

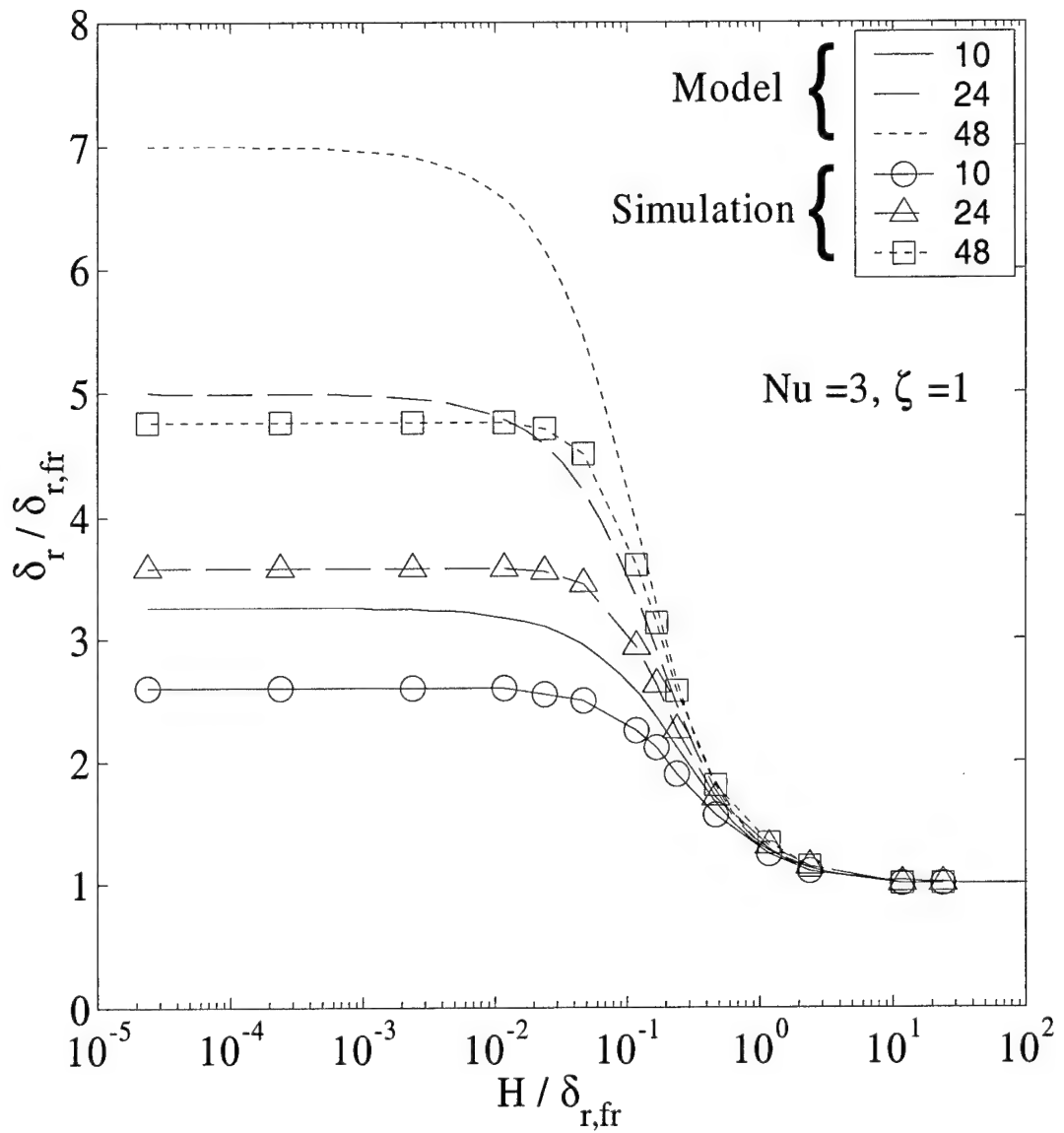


Figure 5: Fractional increase in reaction zone length  $\delta_r$  as a function of the normalized flow passage height  $H/\delta_{r,fr}$  for a range of normalized structure thermal conductivity  $\lambda$ . For the analytical model,  $k_r=0.21$  W/mK. Solid lines correspond to the analytical model and the symbols correspond to numerical model results.

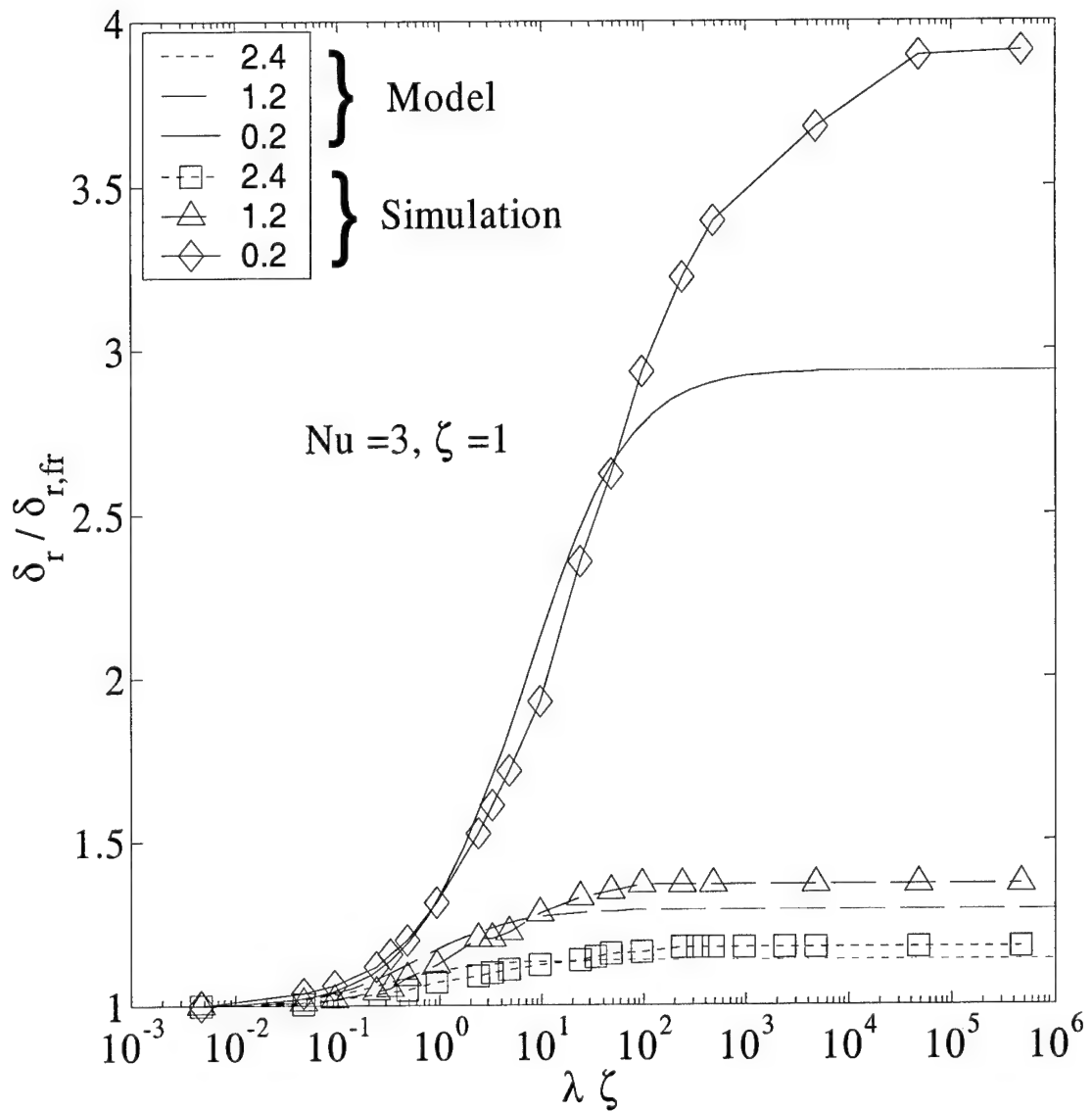


Figure 6: Fractional increase in reaction zone length  $\delta_r$  as a function of non-dimensional thermal conductance ( $\lambda\zeta$ ) of the structure for a range of normalized passage heights.  $\delta_{r,fr}$  is the reaction zone length associated with a freely propagating flame,  $\zeta=1$ ,  $Nu=3$ , and  $k=0.21$  W/mK. Solid lines correspond to the analytical model and the symbols correspond to numerical model results.

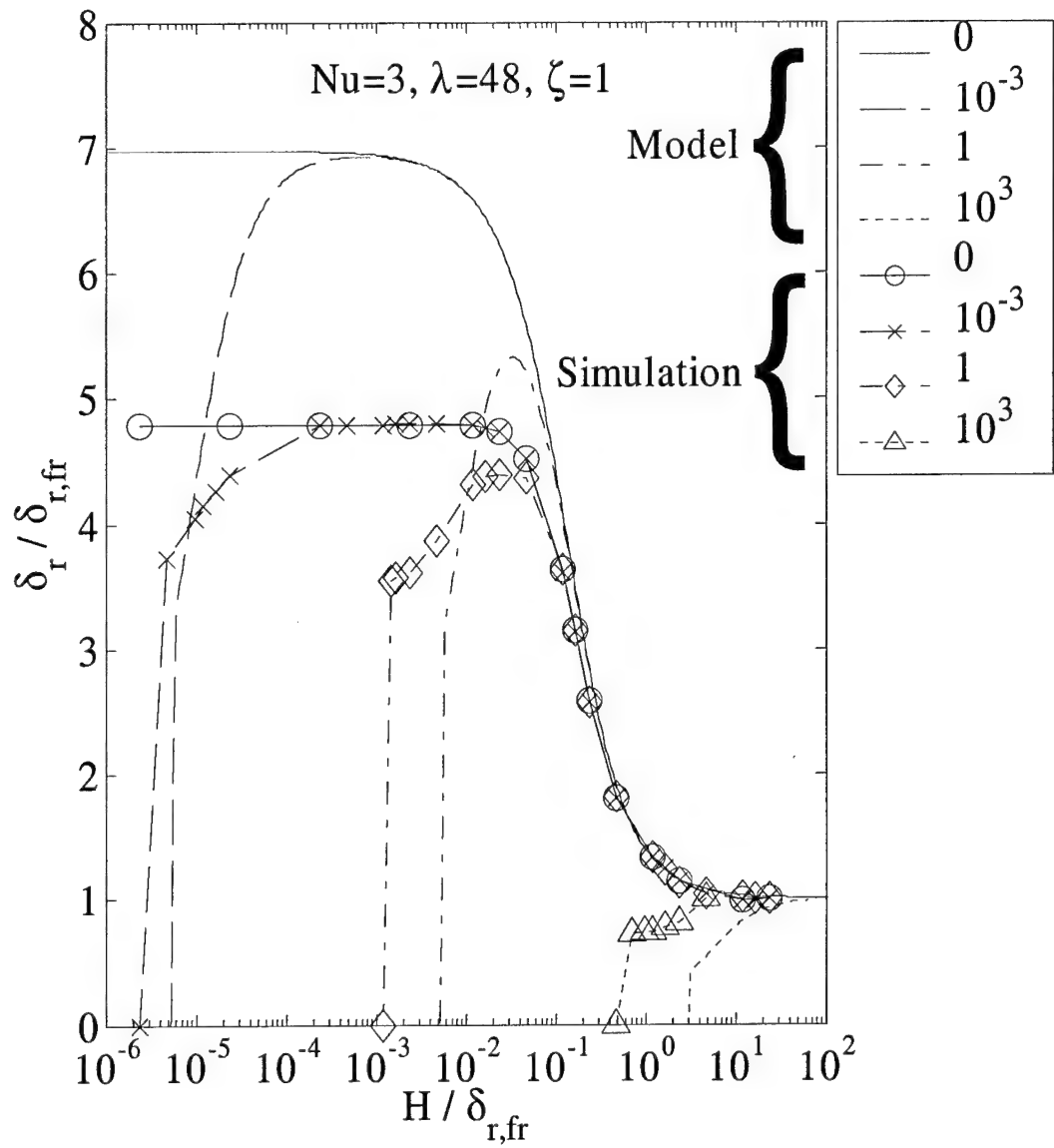


Figure 7: Fractional increase in reaction zone length  $\delta_r$  as a function of the normalized flow passage height  $H / \delta_{r,fr}$  for a range of heat transfer coefficient in  $\text{W/m}^2\text{K}$ . Solid lines correspond to the analytical model and the symbols correspond to numerical model results.

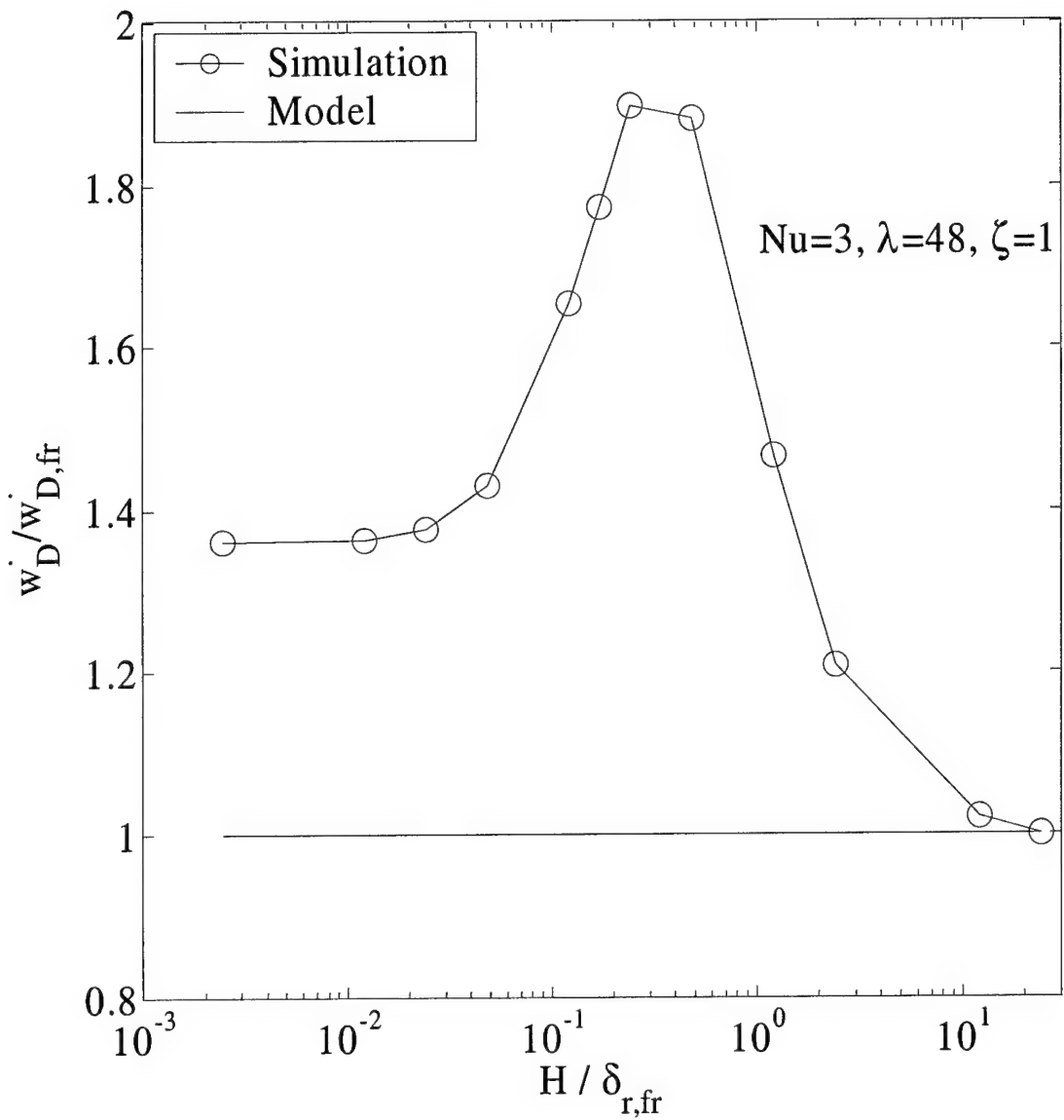


Figure 8: Normalized maximum power density as a function of normalized channel height.

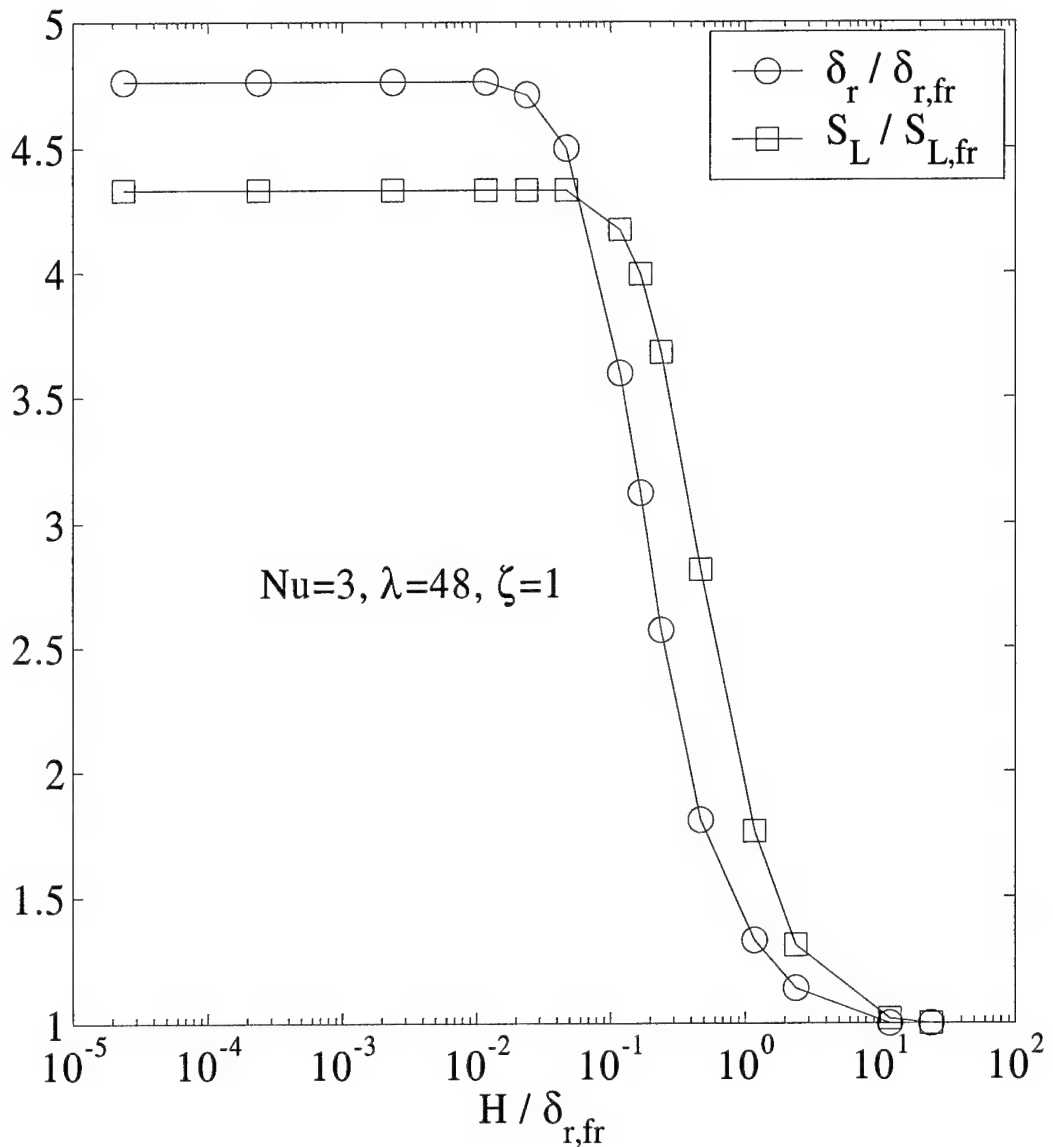


Figure 9: Comparison between the evolution of the normalized flame thickness,  $\delta_r$ , and the normalized laminar flame speed,  $S_L$ .

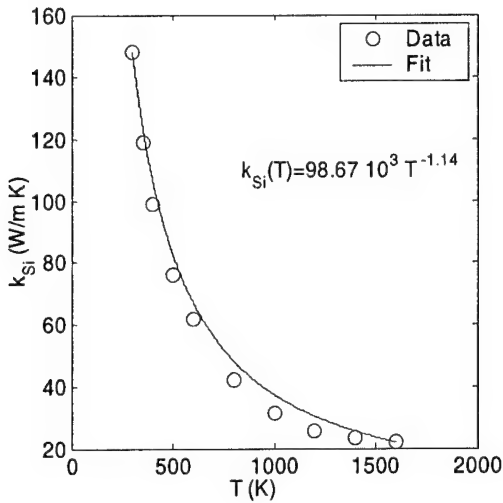


Figure 10: Thermal conductivity of Silicon as a function of temperature [25].

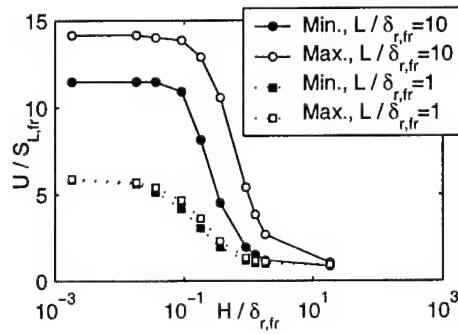


Figure 11: Non-dimensional flashback and blow-off limits for H<sub>2</sub>-air combustion in a silicon micro-channel as a function of non-dimensional channel (combustor) height and for two values of the channel length  $L$ . The equivalence ratio is 0.5 and the pressure is 1 atm.

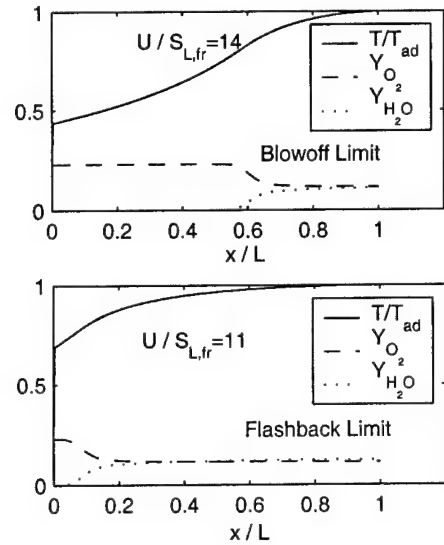


Figure 12: Axial profiles of temperature and major species concentration for a H<sub>2</sub>-Air flame stabilized in a silicon micro-channel with  $H/\delta_{r,fr} = 0.002$  and  $L/\delta_{r,fr} = 9$ . The equivalence ratio is 0.5 and the pressure is 1 atm.

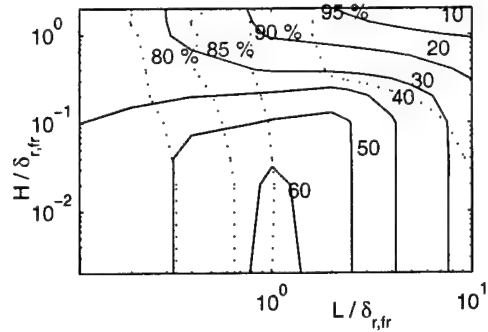


Figure 13: Adiabatic  $\text{H}_2$ -air combustion in a silicon micro-channel;  $\Phi=0.5$ ,  $P=1\text{atm}$ .

Solid lines: Contours of non dimensional power density ( $\dot{w}_D / \dot{w}_{D,ref}$ ) as a function of non-dimensional channel height and length. Dashed lines: Contours of overall efficiency.

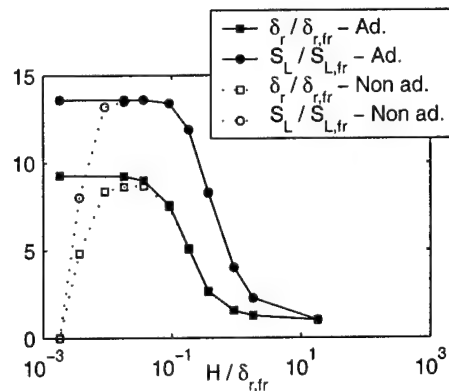


Figure 14: Adiabatic (solid lines) and non-adiabatic (dashed lines)  $\text{H}_2$ -air combustion in a silicon micro-channel;  $\Phi=0.5$ ,  $P=1\text{atm}$ ,  $h_{env}=1 \text{ W/m}^2\text{K}$ ,  $L/\delta_{r,fr}=20$ . The circles show non-dimensional laminar flame speed as a function of non-dimensional channel height while the squares show non-dimensional reaction zone thickness.

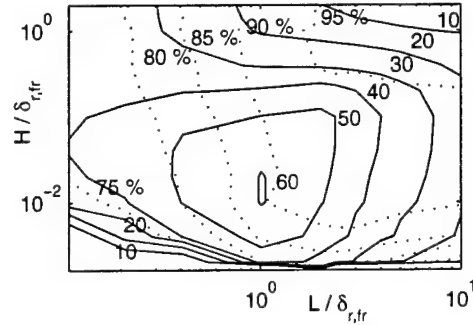


Figure 15: Non-adiabatic  $\text{H}_2$ -air combustion in a silicon micro-channel;  $\Phi=0.5$ ,  $P=1\text{atm}$ ,  $h_{env}=1 \text{ W/m}^2\text{K}$ . Solid lines: Contours of non dimensional power density ( $\dot{w}_D/\dot{w}_{D,ref}$ ) as a function of non-dimensional channel height and length. Dashed lines: Contours of overall efficiency.

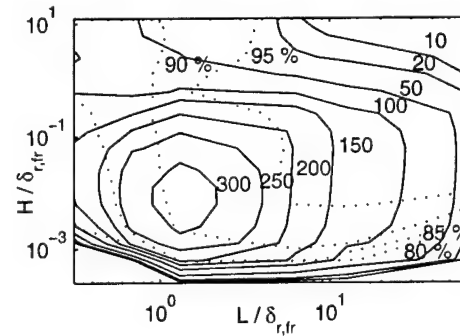


Figure 16: Non-adiabatic  $\text{H}_2$ -air combustion in a silicon micro-channel;  $\Phi=0.5$ ,  $P=5\text{atm}$ ,  $h_{env}=1 \text{ W/m}^2\text{K}$ . Solid lines: Contours of non dimensional power density ( $\dot{w}_D/\dot{w}_{D,ref}$ ) as a function of non-dimensional channel height and length. Dashed Lines: Contours of overall efficiency.

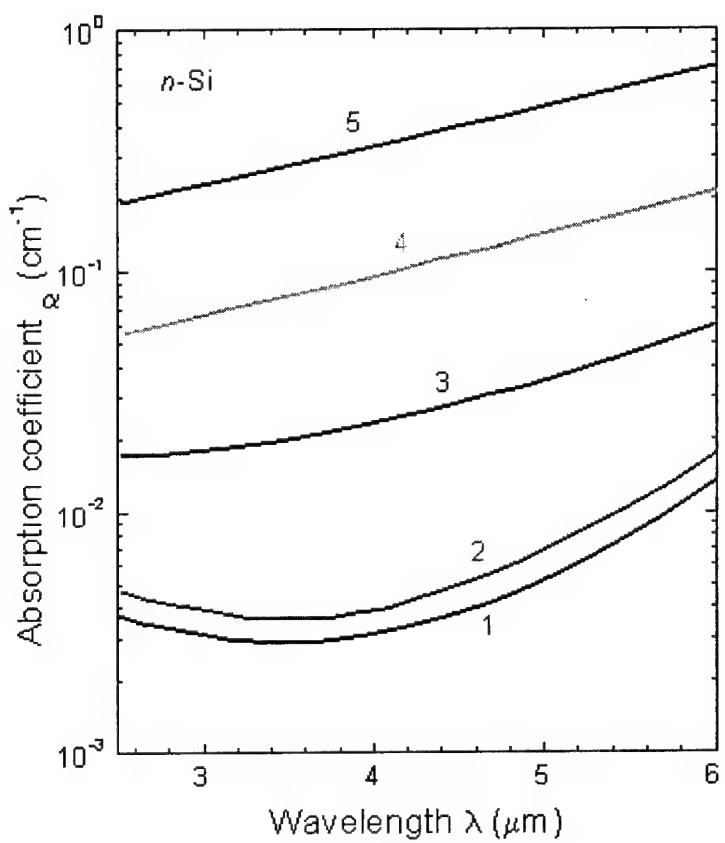


Figure 17 Free carrier absorption versus wavelength for high purity silicon. Temperatures are 1. 300 K; 2. 473 K; 3. 573 K; 4. 623 K; 5. 673 K. Data from [32]

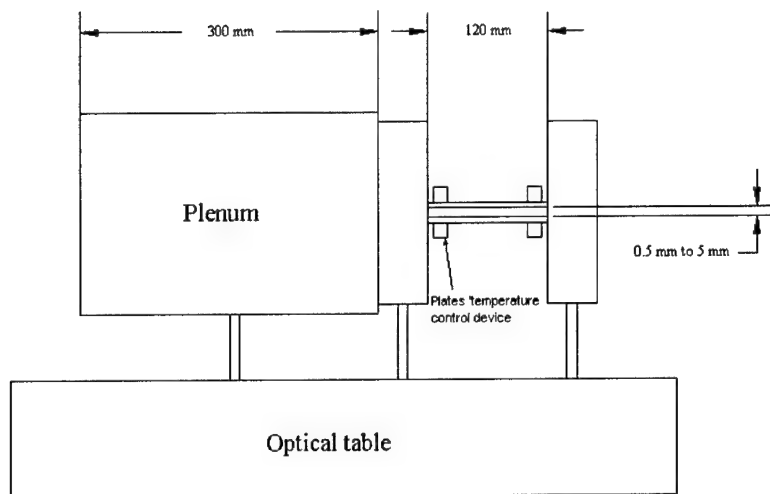


Figure 18. Diagram of parallel plate flow reactor showing overall layout.

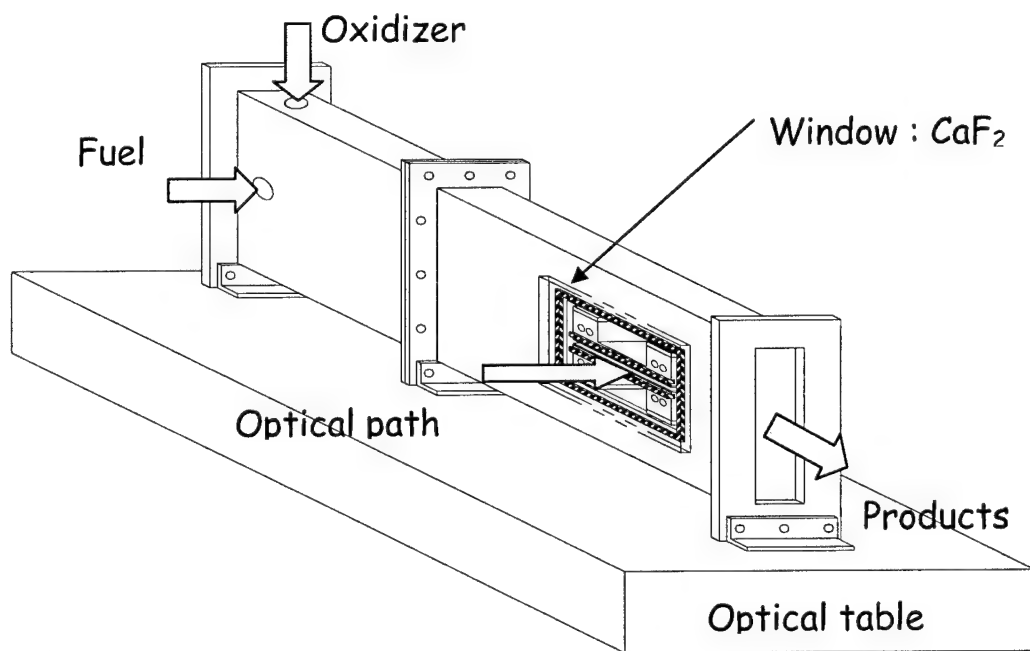


Figure 19. Schematic diagram of reactor showing introduction of reactants and the general optical path.

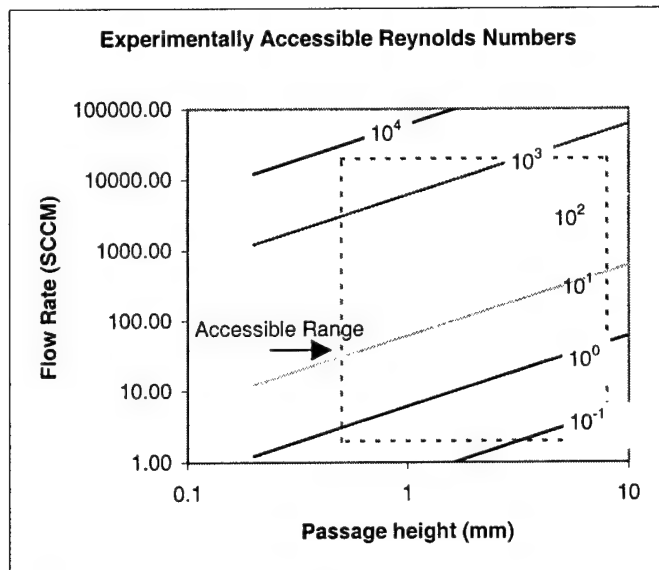


Figure 20 Reynolds numbers available in flow facility

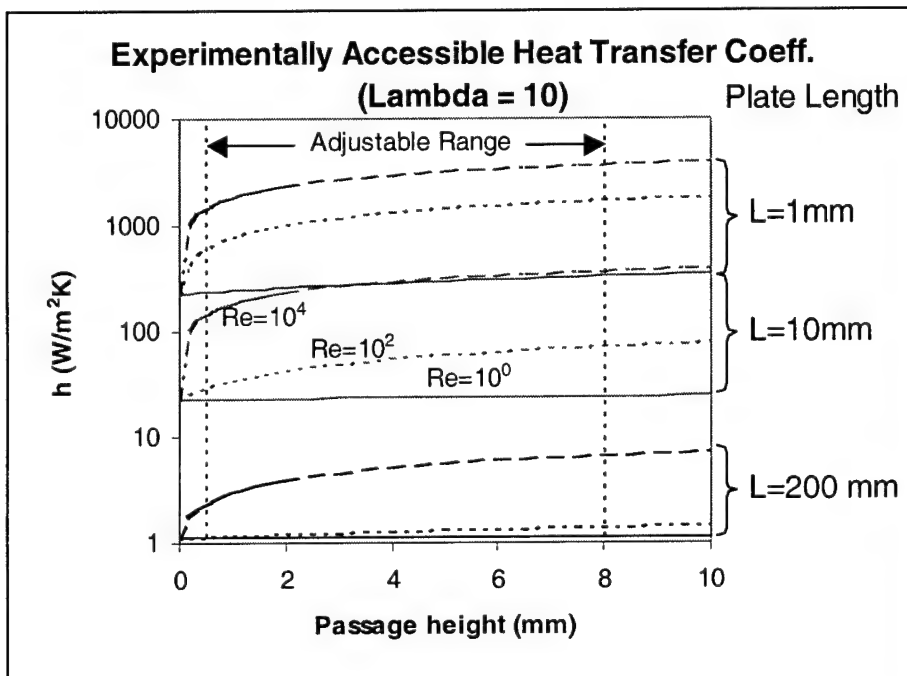


Figure 21 Heat transfer coefficients available in flow facility

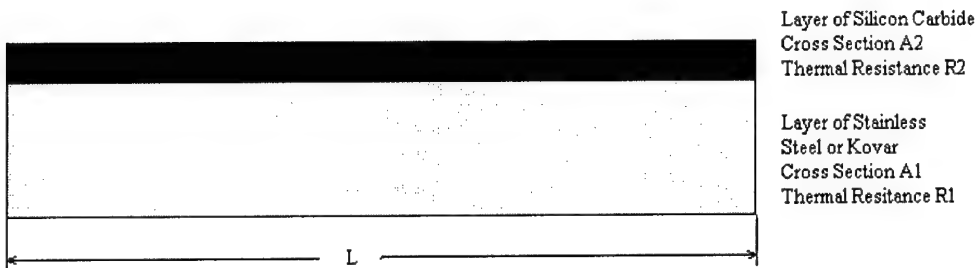


Figure 22 Cross section of the plates

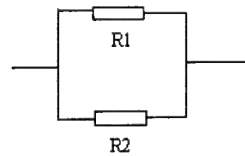


Figure 23 Equivalent electrical diagram for the substrate and coating of the combustor side plates.

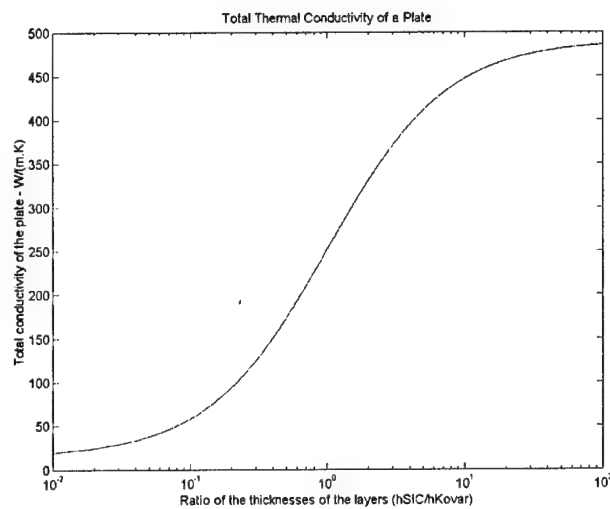


Figure 24 Effective thermal conductivity of the composite plate

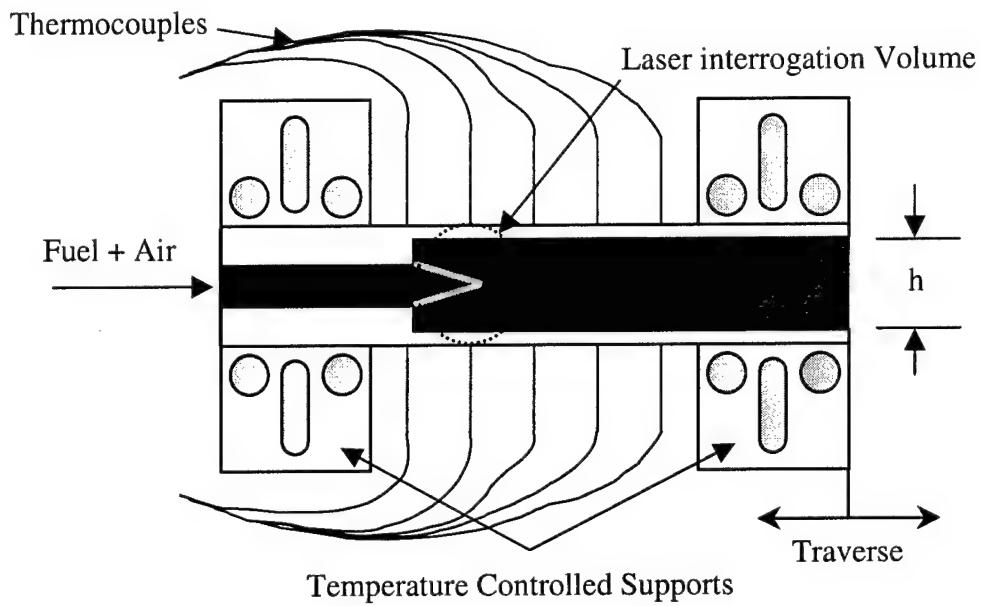


Figure 25. Schematic diagram of temperature-controlled supports for parallel plate flow reactor.

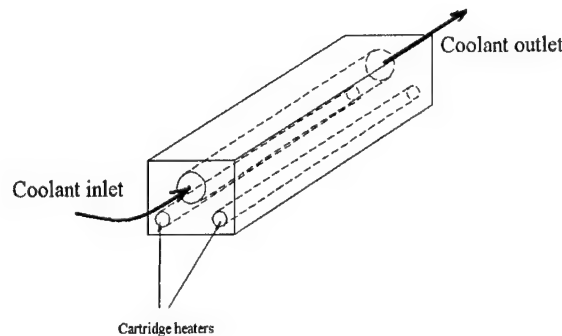


Figure 26. Coolant flow path through temperature controlled support.

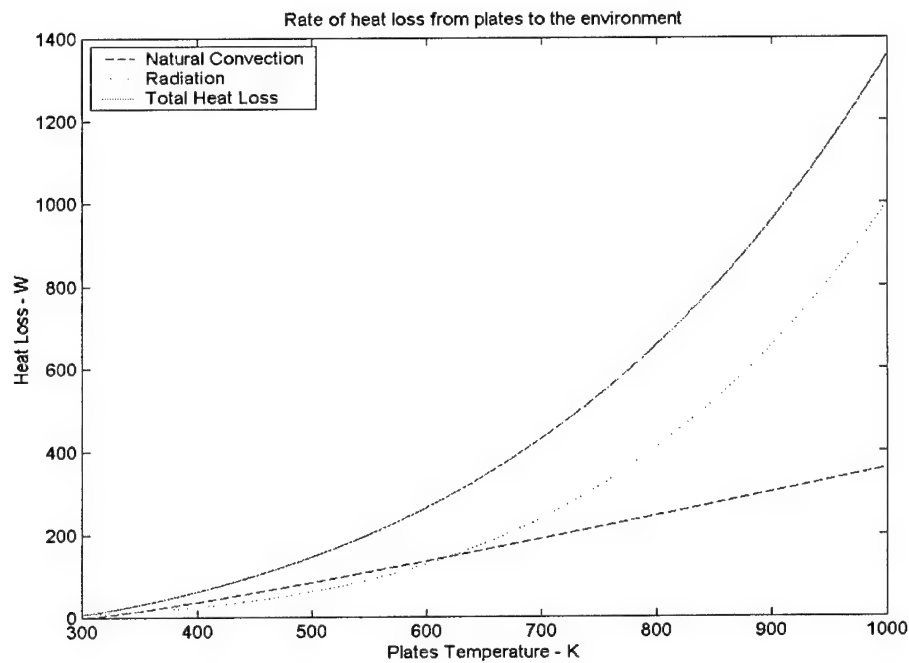


Figure 27 Heat loss from the test section to the environment (worst-case)

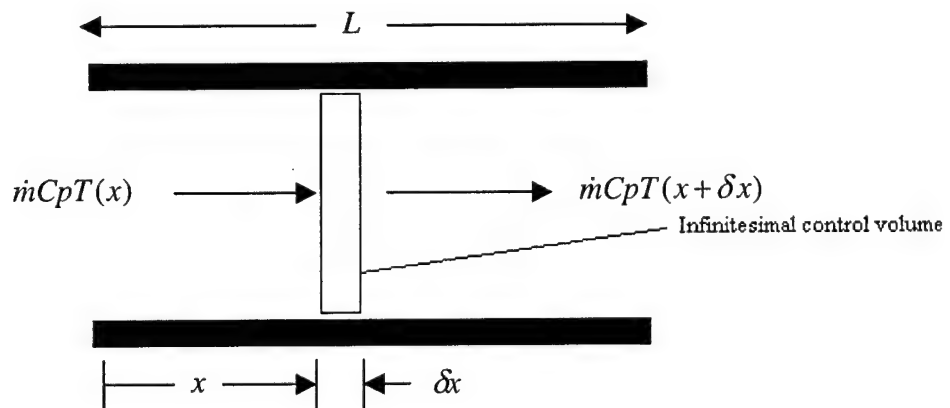


Figure 28. Control volume for thermal analysis

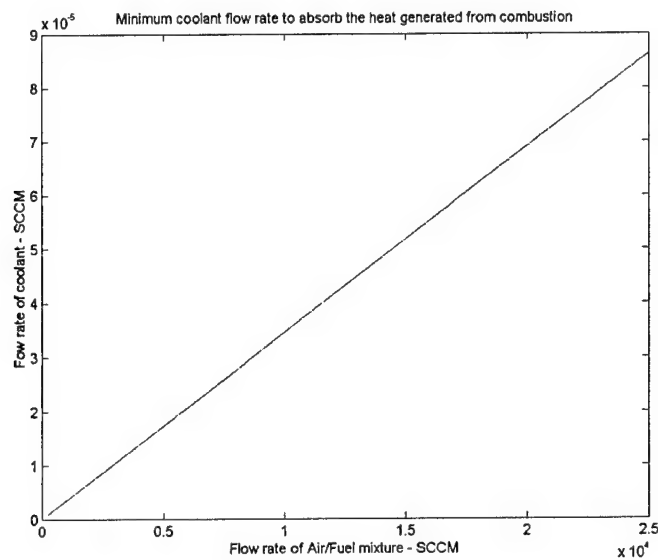


Figure 29 Minimum flow rate of coolant required to absorb heat of combustion

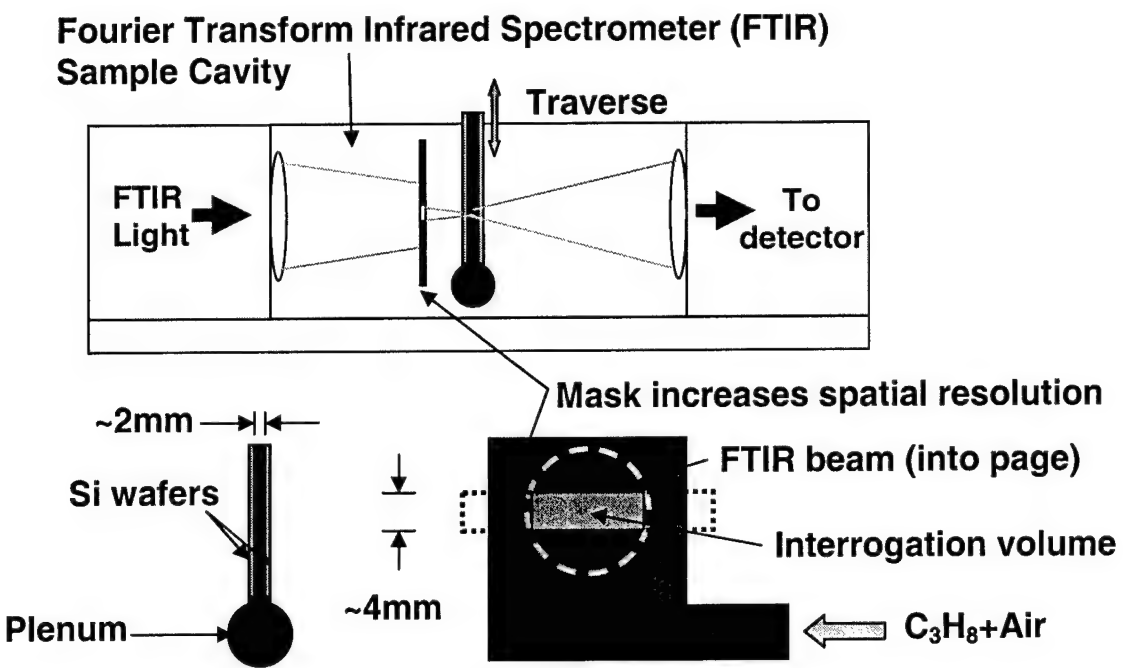


Figure 30. Schematic diagram of proof-of-concept experiment for infrared diagnostics.

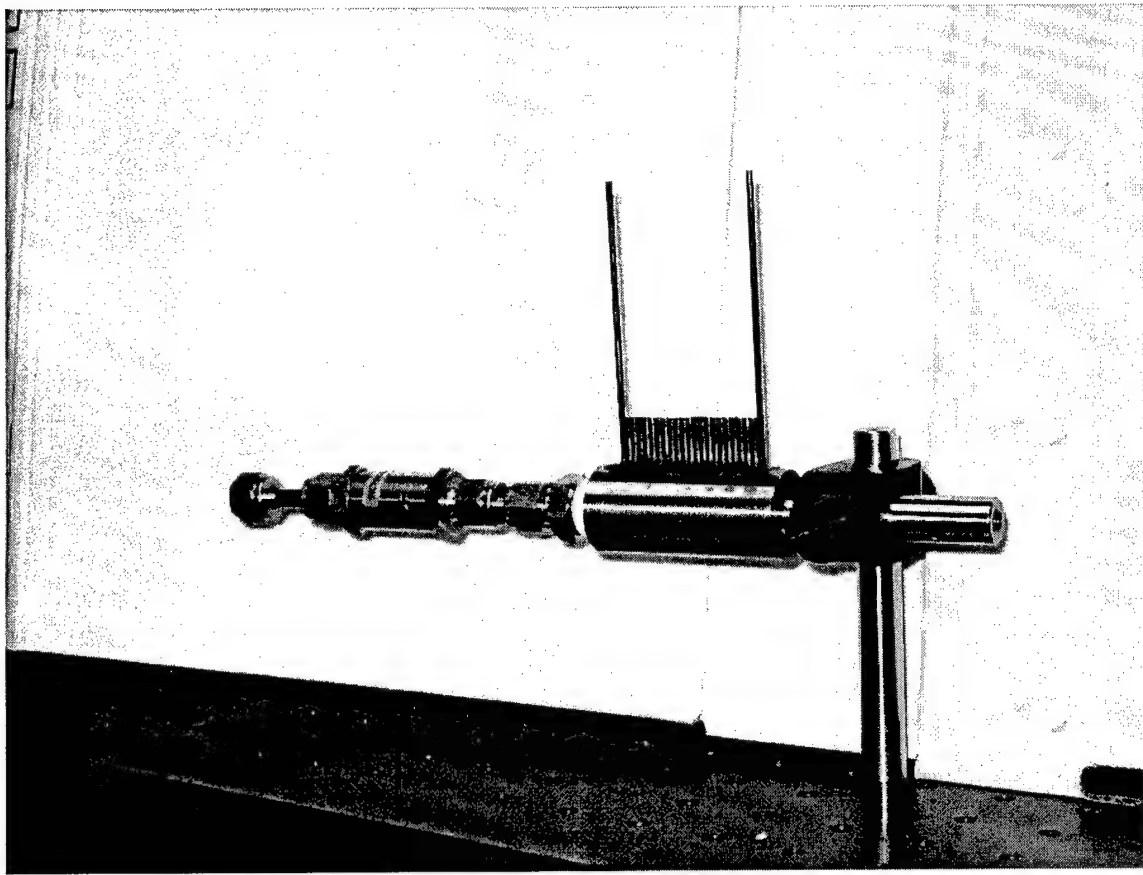


Figure 31. Photograph of silicon-walled micro-combustor with silicon wafers removed to show the fuel plenum and delivery tubes.

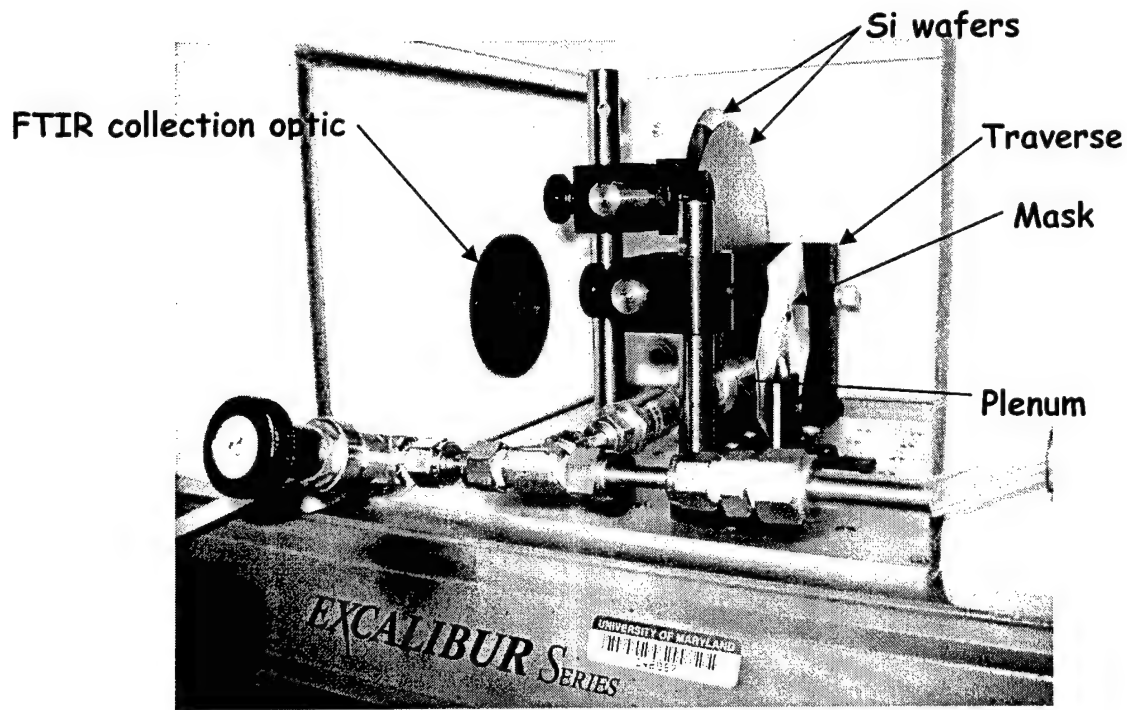


Figure 32. Silicon-walled micro-combustor installed in FTIR sample compartment.

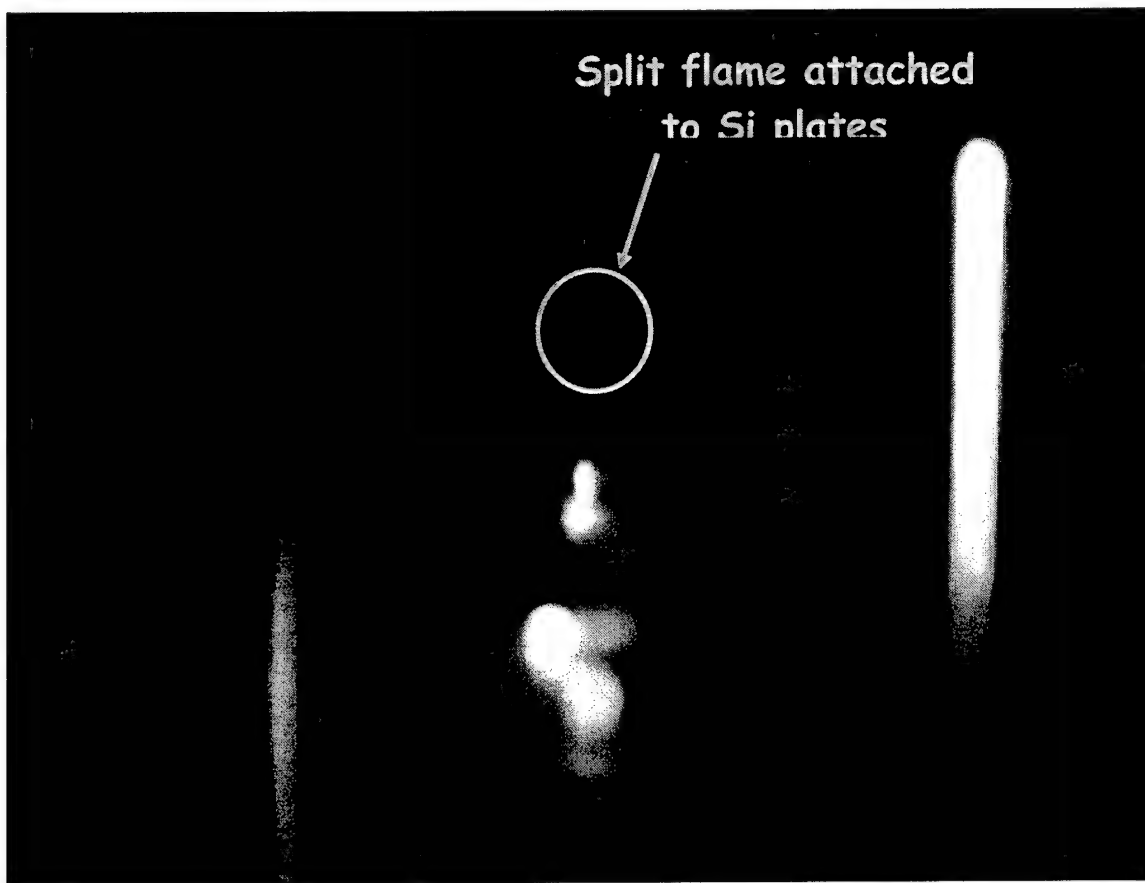


Figure 33. Photograph showing a side view of the silicon-walled micro-burner. Note that the flame is 'split' and is attached to both the right and left silicon plates.

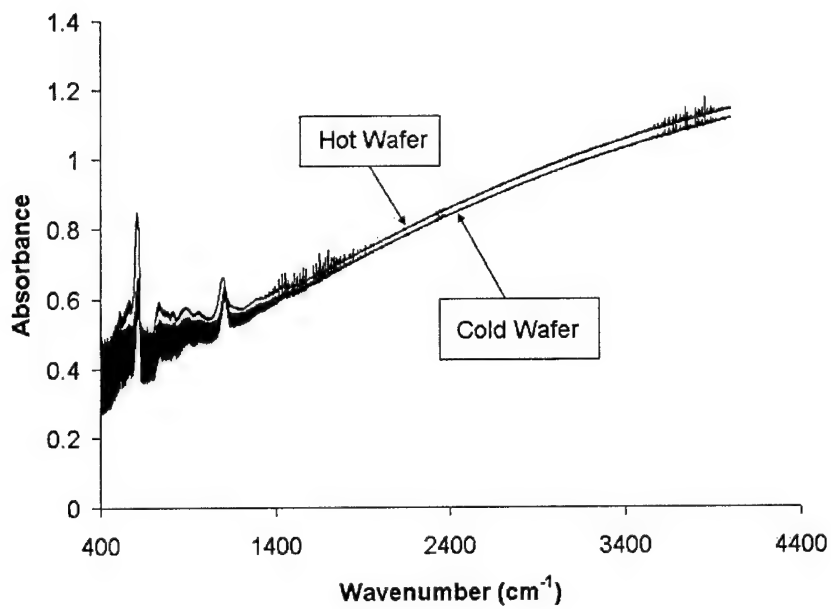


Figure 34. Absorbance of a hot (~400 K) and cold (room temperature) silicon wafer.

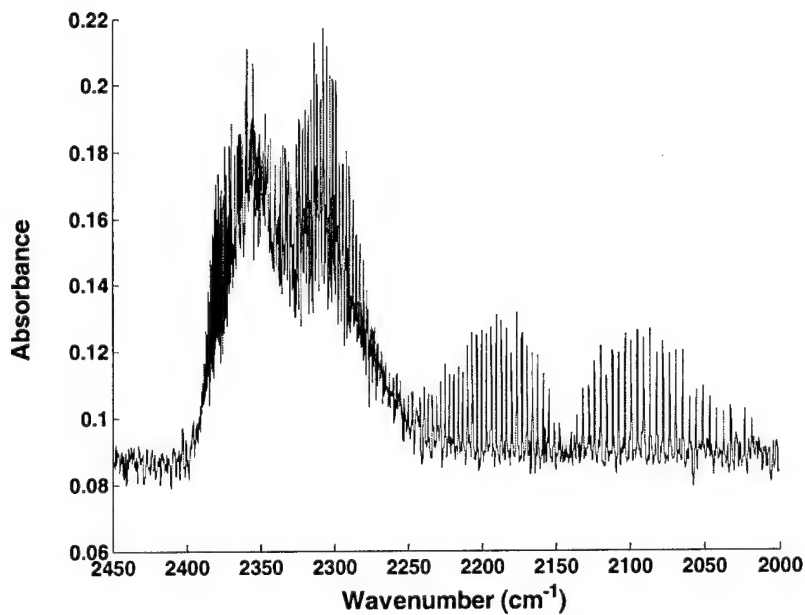


Figure 35. Typical spectra of CO and CO<sub>2</sub> acquired in the silicon-walled micro-combustor

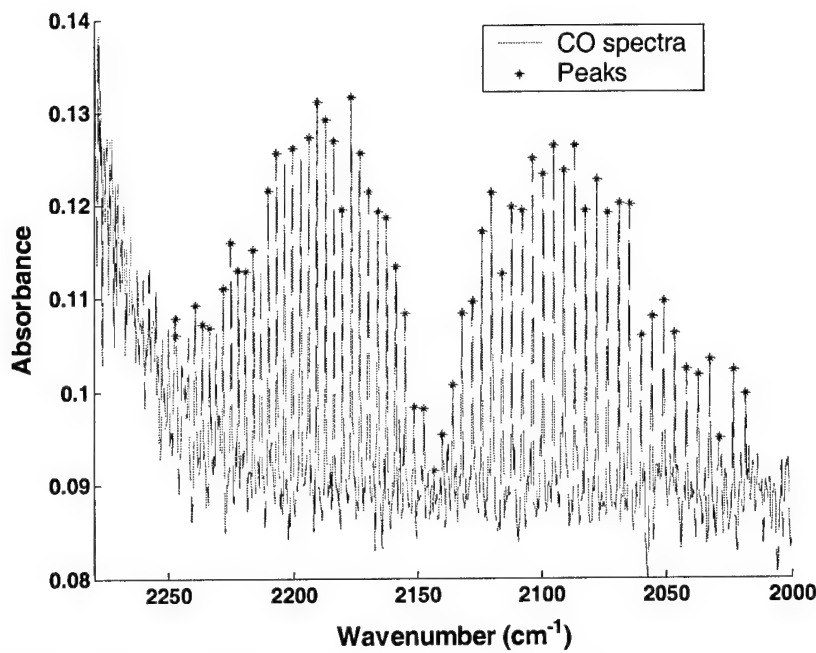


Figure 36: Identification of CO peaks at room temperature.

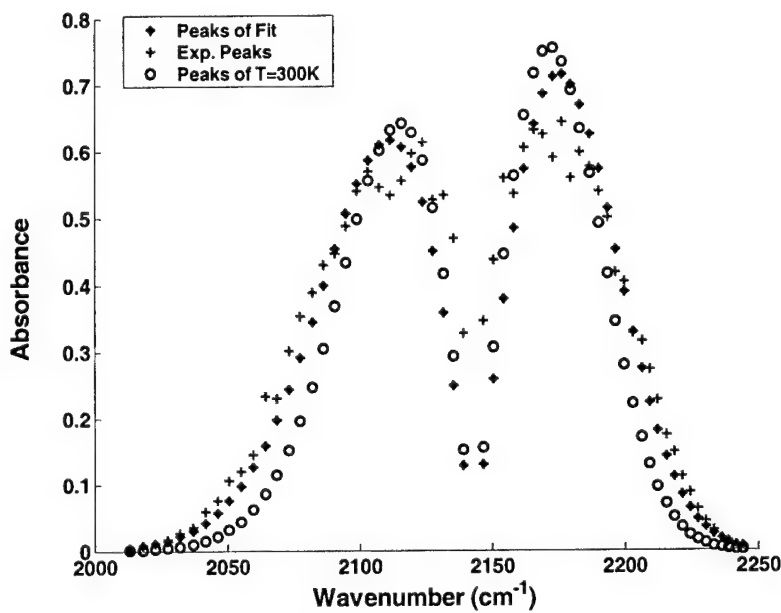


Figure 37 - Room temperature calibration spectrum best fit to theoretical spectrum (388K) and 300K theoretical spectrum.

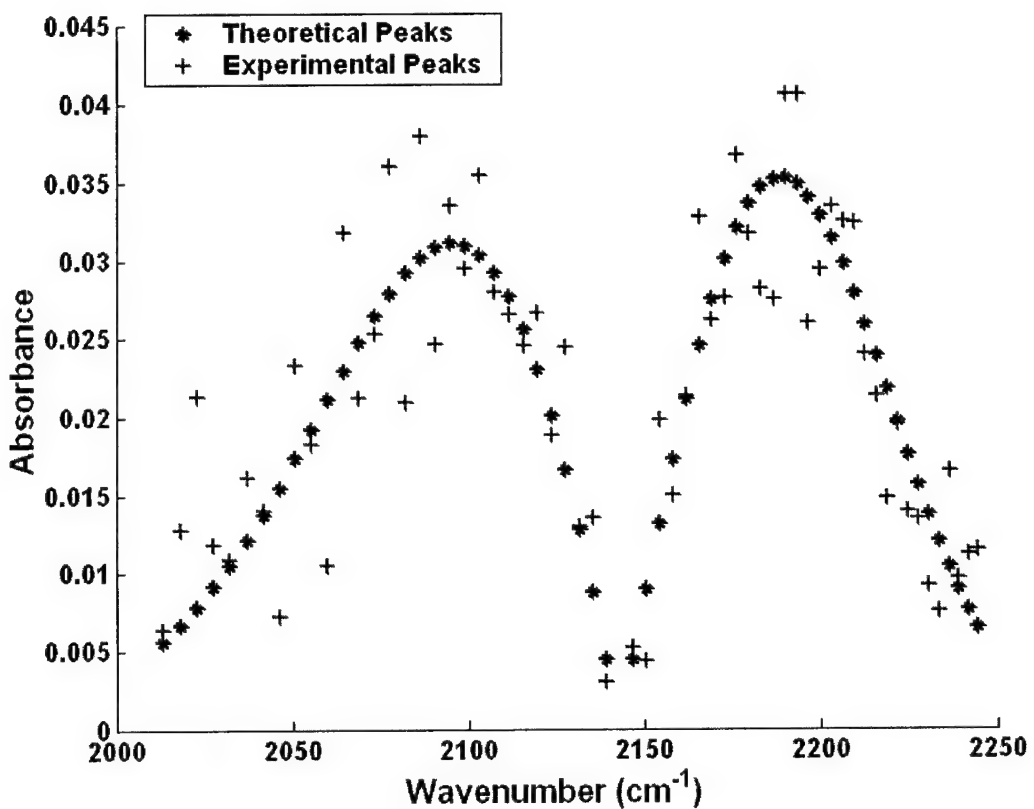


Figure 38 – Fit of CO high temperature experimental data taken 9 mm downstream of the flame. The best-fit temperature is 829K.

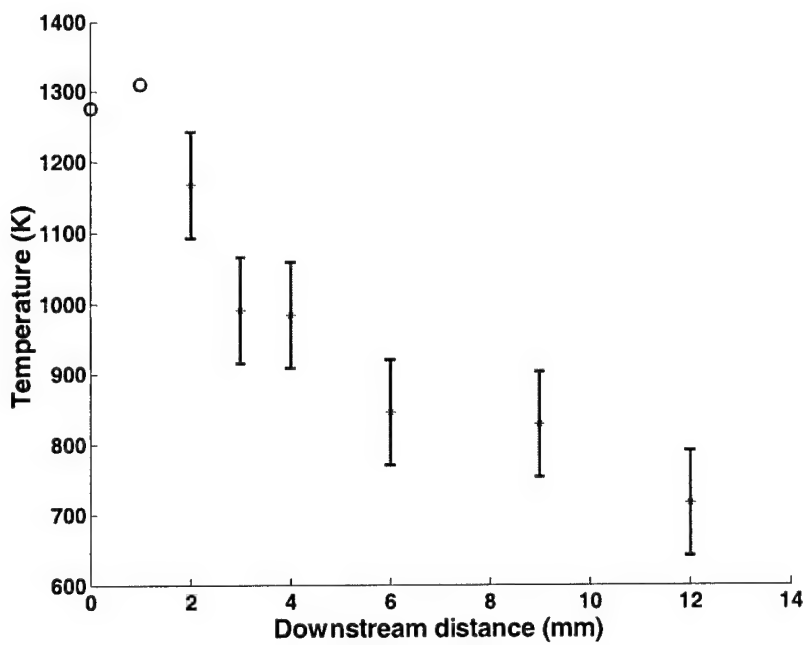


Figure 39 – Temperature vs. downstream distance derived from CO spectra.

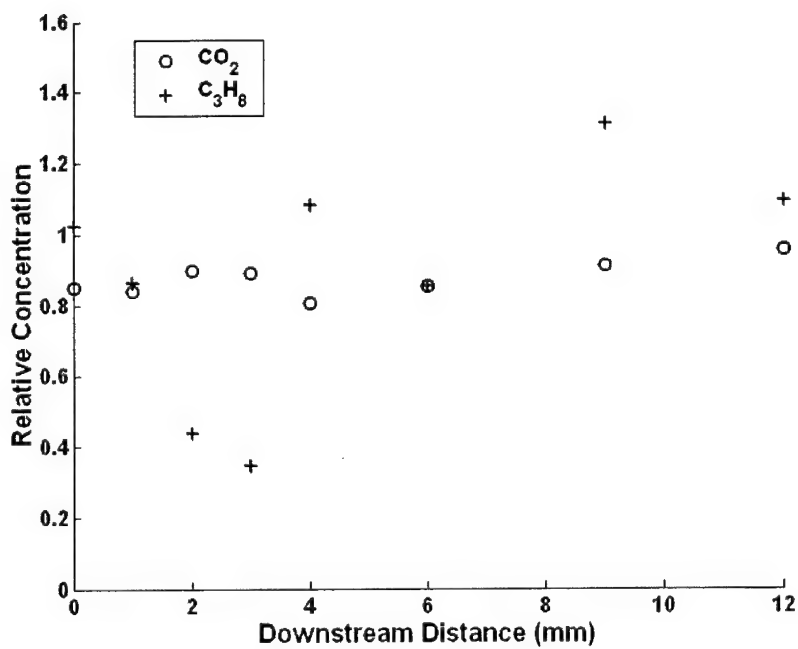


Figure 40 – Relative CO<sub>2</sub> and propane concentrations vs. downstream distance.

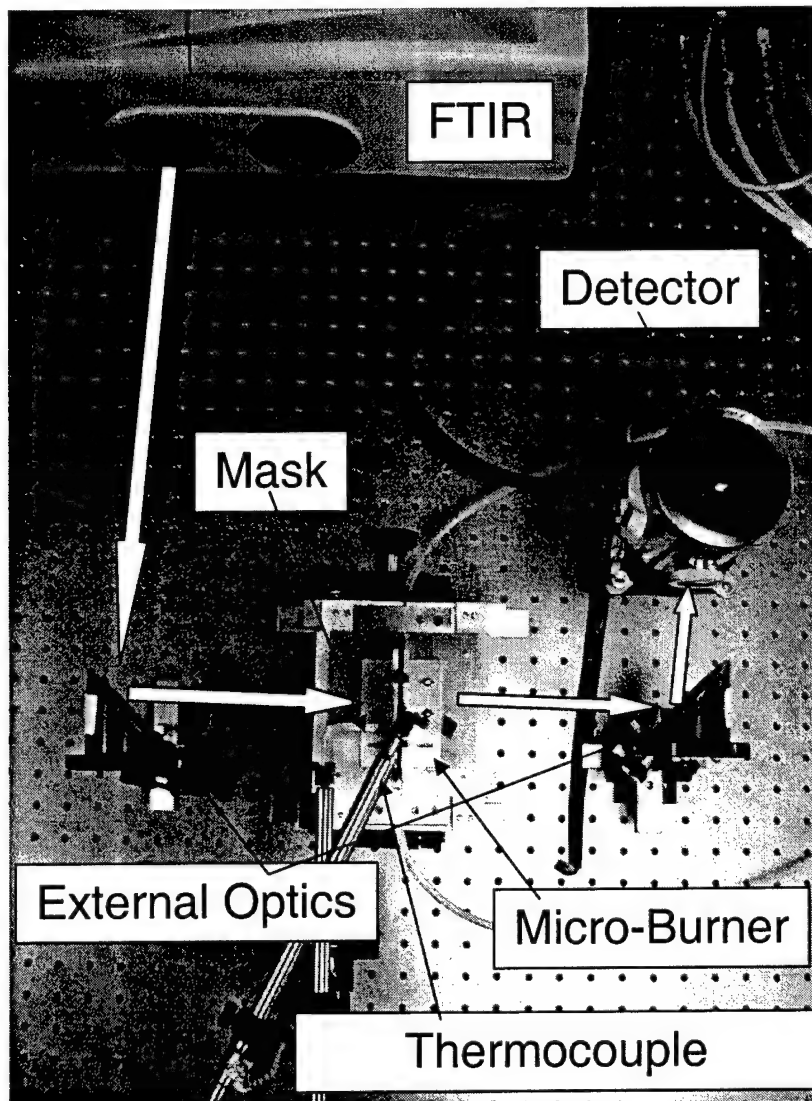


Figure 41. Top view of improved 'second generation' experiment

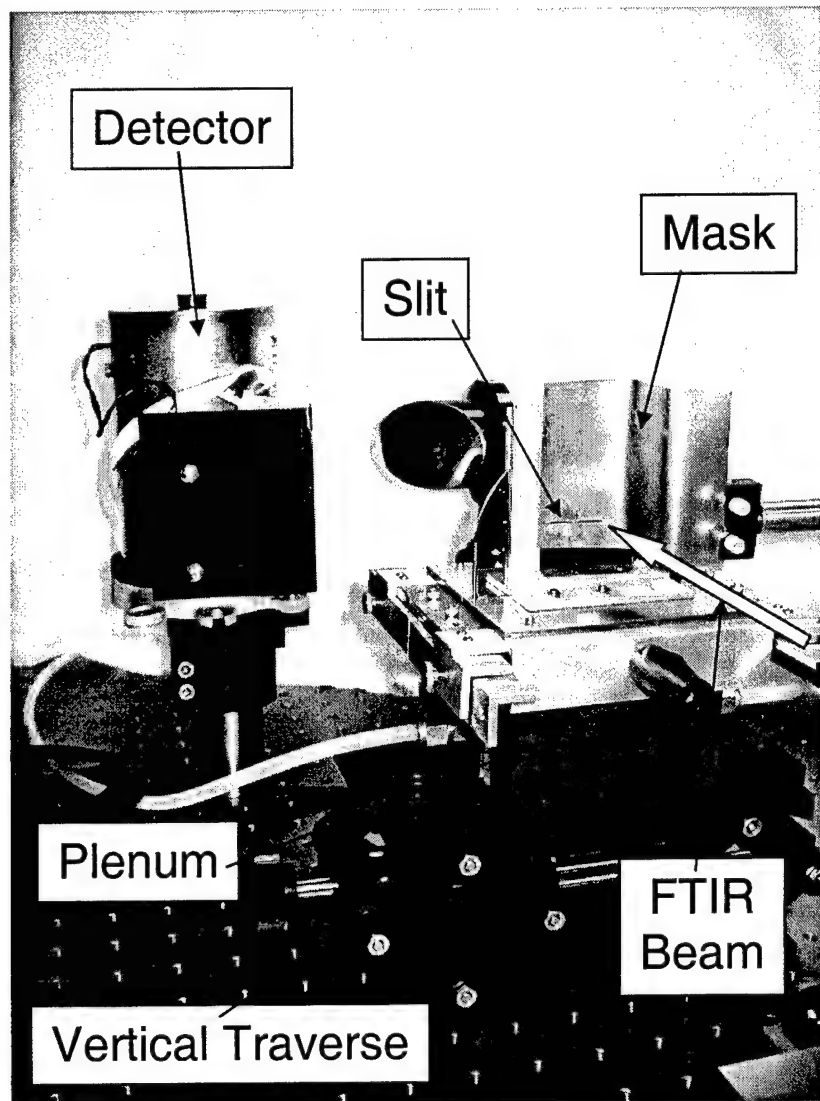


Figure 42. Side view of improved 'second generation' experiment

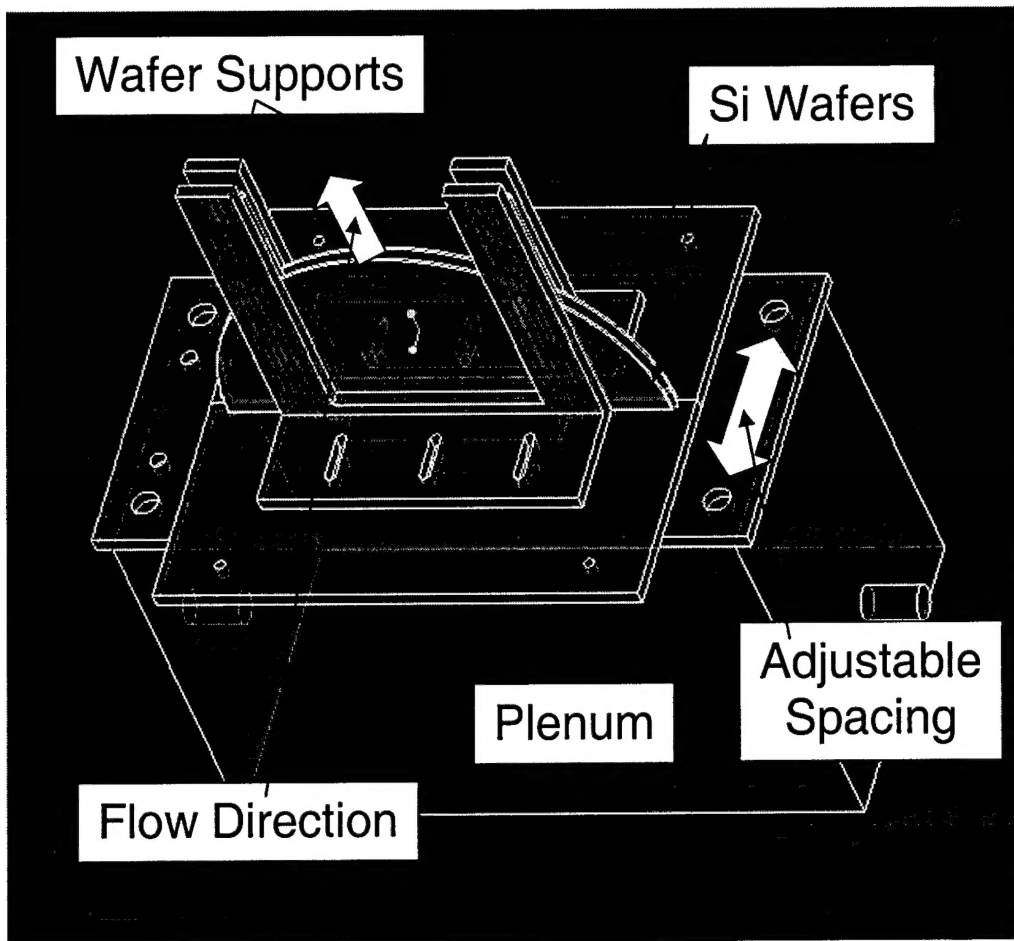


Figure 43. Schematic diagram of second generation micro-burner

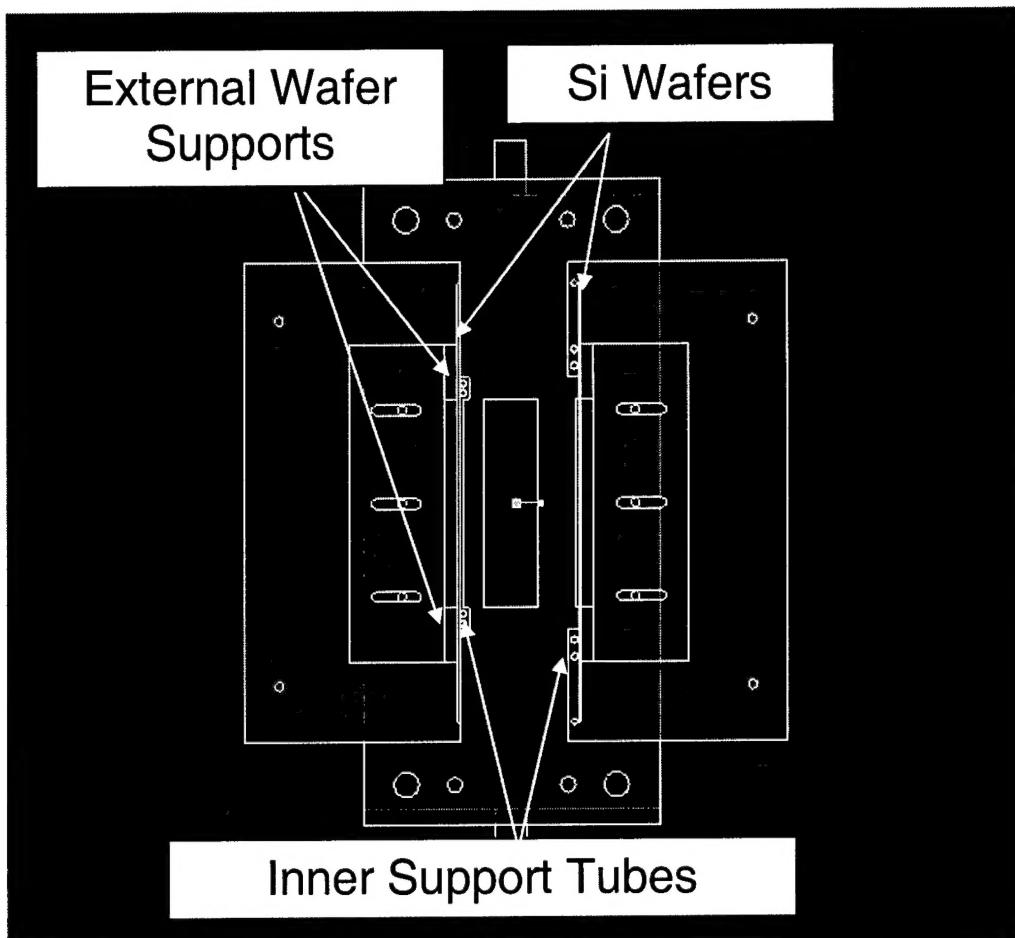


Figure 44. Top view of second generation micro-burner showing silicon wafers in retracted position corresponding to a large passage height.

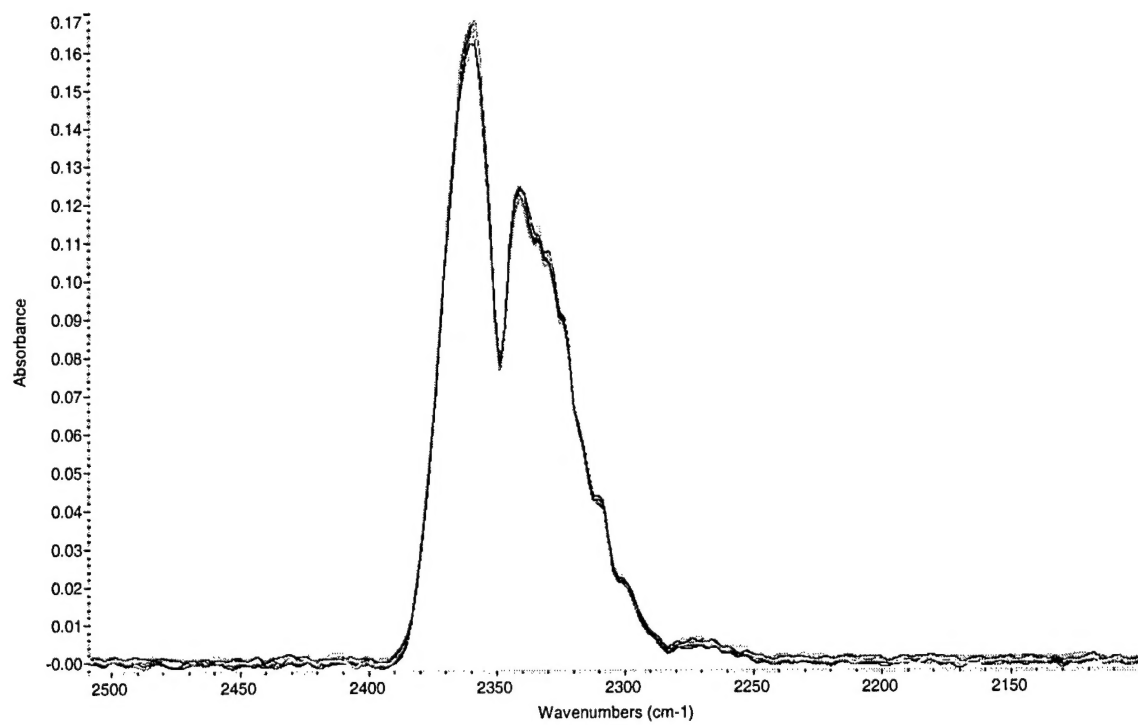


Figure 45. Absorption band of CO<sub>2</sub> acquired in the second-generation micro-burner

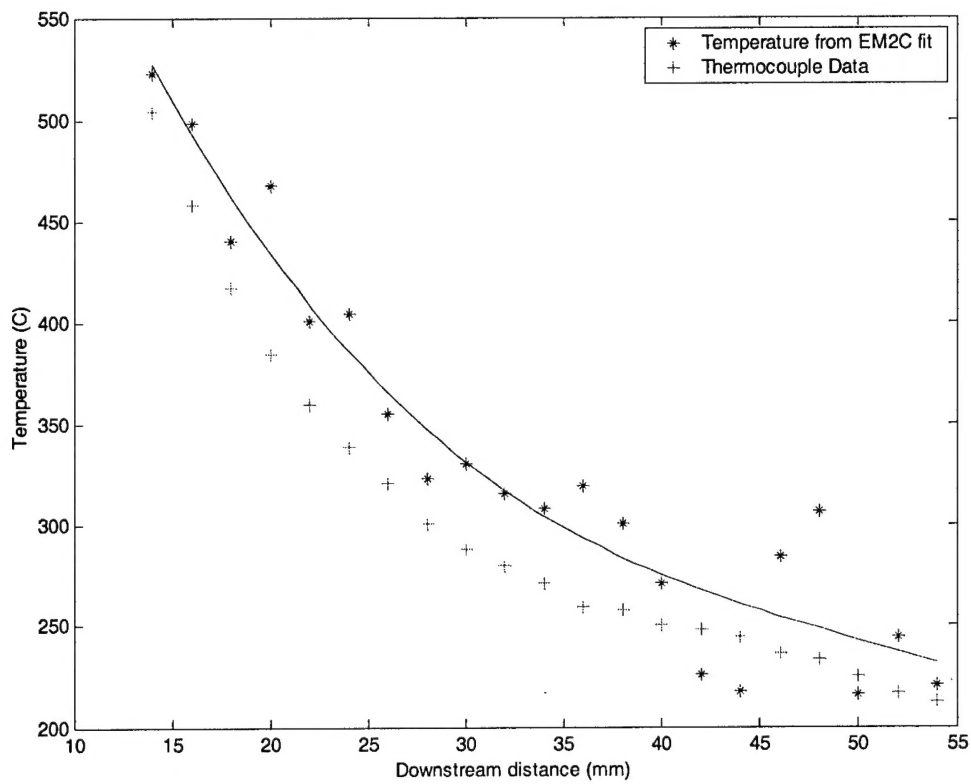


Figure 46. Temperature as a function of downstream distance in the second generation micro-burner. The stars are preliminary temperature estimates based on the vibrational structure of the  $\text{CO}_2$  band, and the crosses correspond to uncorrected K-type thermocouple measurements.